
LUNDS UNIVERSITET

Lund University
Faculty of Engineering
Division of Solid State Physics

# Towards a Cooper pair splitter in InAs nanowires with crystal-phase defined quantum dots

A Thesis Submitted for the Degree of Master of Science in Engineering, Engineering Physics

**Supervisor:** Assoc. Prof. Claes Thelander
**Co-supervisor:** Markus Aspegren
**Examinator:** Assoc. Prof. Carina Fasth

**Author:**
Louise Olausson

June 2022

## Acknowledgements

I would like to show my immense gratitude to those who have supported me during my time at the division of Solid State Physics. The completion of this thesis would never have been possible without you.

First, I would like to thank my main supervisor Claes Thelander for his incredible support as well as the expertise and ideas he provided during the project. I would also like to thank Claes for his patience and for spending too many hours with me in the lab. Thank you for giving me the opportunity to pursue this thesis and for introducing me to the fascinating world of experimental quantum physics.

I would also like to thank my co-supervisor Markus Aspegren for his support and the help he has given me during fabrication and measurements. Thank you for the valuable explanations that have deepened my theoretical understanding.

Finally, I would like to thank Rousan Debbarma and Sebastian Lehmann for continuous encouragement and fruitful discussions during my project. Thank you Rousan for guiding me how I should conduct my measurements and interpret the results. And thank you Sebastian for valuable inputs and for growing the nanowires used in the project.

Once again, this work would never have been possible without the fantastic support I have received from all of you.

# Abstract

Cooper pair splitting (CPS) is a process in which the two spin-entangled electrons of a Cooper pair in a superconductor are split into two spatially separated electrons. If the separated electrons are still entangled, CPS can be studied to increase the knowledge of non-locality in quantum systems. This thesis is a first step towards the realization of CPS in InAs nanowires with crystal-phase defined quantum dots. Previous studies with these nanowires have shown that it is possible to control the spin-ground state with the help of small electric and magnetic fields. If CPS also is possible in these nanowires, this may in the future lead to new opportunities for spin-resolved CPS, which opens a route towards a test of the Einstein-Podolsky-Rosen (EPR) paradox and Bell's inequality.

The nanowires studied in this thesis had a shell of GaSb to improve contact alignment. Good contact alignment was important in this project since the superconducting contact must be placed very close to the quantum dots, in order for the superconductivity to be induced into the nanowire via the proximity effect. The shell of GaSb was removed prior to metal evaporation by a wet-etch in the developer MF319. To improve the quality of the InAs-Ti/Al contact interface, two different processing schemes were developed and compared. The quality of the contact interface became better if the whole GaSb shell was removed before any other process step than if the GaSb was removed in two separate steps. It was also found that $H_2O$ also can be used to etch GaSb.

The search for experimental signatures of CPS was performed at mK temperatures in a dilution refrigerator. A CPS signal can potentially be very weak and difficult to isolate from a noisy background. Therefore, several comparisons between standard DC measurements and AC measurements with a lock-in amplifier were performed, where one research question was to determine which measurement technique is most suitable for detecting CPS. One important topic of study was finding out how a setup can generate non-local signals. This can occur in DC measurements due to a DC offset between amplifiers, as is shown in this work. The non-local signal will look like a CPS signal but can remain even when the contact is no longer superconducting.

Some of the advantages of DC measurements are instead that they are, in general, faster and simpler to perform since they do not need significant settings optimization. AC measurements, on the other hand, require that settings such as reference frequency and root-mean square voltage are selected appropriately. These settings were most likely not well selected for the various measurements performed in this thesis since the AC measurements resulted in broader features and lower signals than the corresponding DC measurements. A conclusion from this thesis is that it can be difficult to make good AC measurements, but they have the advantage of eliminating the problem with DC offsets and should therefore be used when studying CPS to reduce the risk of other non-local signals.

The ultimate goal of this thesis was to observe experimental signs of CPS, but no such signs could be confirmed. The primary reason for this was probably a too long distance between the quantum dots. The width of the superconducting contact of 400 nm was likely too wide compared to the coherence length in diffusive aluminum nanostructures which typically lie in the range of 100 to 200 nm.

## Populärvetenskaplig sammanfattning

Det är intressant att studera om de spinn-sammanflätade elektronerna i ett Cooperpar kan delas upp, eftersom detta förutspås kunna användas när man bygger kvantdatorer. En kvantdator kan lösa vissa problem som vanliga, klassiska datorer inte kan och kan dessutom lösa en del problem snabbare. En ökad kunskap om kvantfenomen på ett fundamentalt plan är en förutsättning för vidare kvantteknologisk utveckling, vilket på sikt kan bidra till nya tillämpningar.

Spinn är en egenskap hos en elektron som endast kan anta två olika värden, spinn upp eller spinn ned. Två elektroner kan vara spinn-sammanflätade, vilket betyder att om man mäter spinnet för den ena elektronen kan man omedelbart bestämma spinnet för den andra elektronen. Ett Cooperpar består av två spinn-sammanflätade elektroner med motsatt spinn och finns i supraledande material under en viss kritisk temperatur. I detta arbete undersöktes om elektronerna i ett sådant par kunde delas upp enligt strukturen i Figur 1. En ström av Cooperpar leddes från en supraledande kontakt, S, till en nanotråd med två kvantprickar, QD1 och QD2. Vardera kvantprick var i kontakt med en normal ledare, N1 och N2. I figuren är elektronerna ritade som svarta prickar med pilar för att symbolisera riktningen på spinnet.

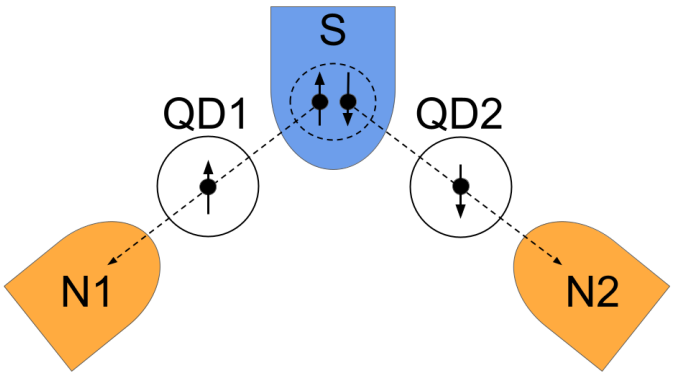


Figur 1: Supraledande kontakt, S, kvantprickar, QD1 och QD2, samt normala kontakter, N1 och N2. Elektronerna är ritade som svarta prickar med pilar för att symbolisera riktningen på spinnet. Den streckade cirkeln symboliserar att de två elektronerna är ett Cooperpar.

Två elektroner tycker inte om att vara nära varandra eftersom de har samma laddning. I en kvantprick tvingas elektronerna att vara instängda i ett väldigt litet område, vilket gör att de inte vill åka igenom en kvantprick samtidigt. Därför bidrar kvantprickarna till att dela upp elektronerna i Cooperparet.

Nanotrådar är små nålliknande strukturer med en diameter på 10-100 nanometer och en längd på några få mikrometer och var i detta arbete gjorda av halvledarmaterialet indiumarsenid (InAs) med ett skal av galliumantimonid (GaSb). I nanotrådarna fanns två kvantprickar som uppstod på grund av att nanotråden bestod av två olika kristallstrukturer som kallas wurtzit och zinkblände. GaSb växer endast på InAs av zinkblände vilket gjorde det enkelt att se var segmenten av wurtzit fanns. Detta är viktigt eftersom den supraledande kontakten måste placeras mycket nära kvantprickarna. En illustration av en nanotråd kan ses i Figur 2a. I figuren syns också en partikel av guld (Au) som användes när nanotrådarna växtes. Skalet av GaSb togs bort av kemikalien MF319 före kontakterna lades på. De normala kontakterna tillverkades av nickel/guld (Ni/Au) och den supraledande kontakten av titan/aluminium (Ti/Al). Det tillverkades också en sidokontakt, sg, av Ti/Al. Den färdiga strukturen med pålagda kontakter kan ses i Figur 2b.

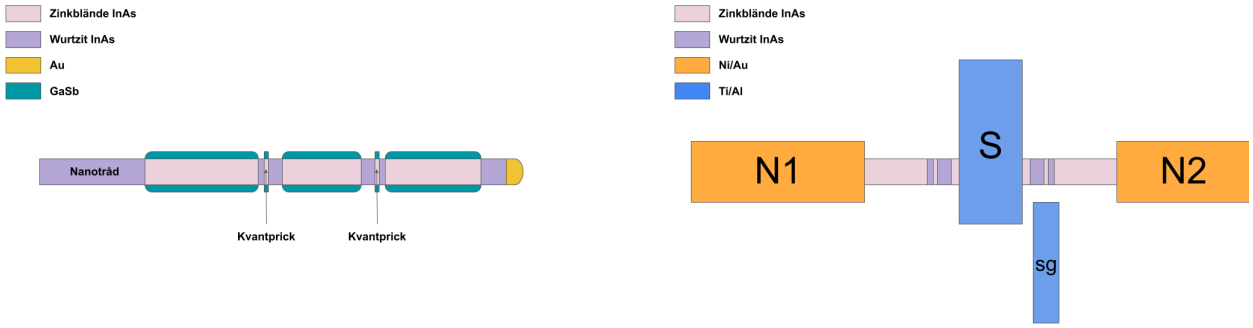


(a) Nanotråd av InAs med zinkblände kvantprickar och skal av GaSb.

(b) Nanotråd med supraledande kontakt, S, sidokontakt, sg, samt två normala kontakter, N1 och N2.

Figur 2

För att få en bra kvalité på ytan mellan den supraledande kontakten och nanotråden jämfördes två olika processmetoder. Det visade sig att om hela GaSb-skalet på nanotråden togs bort före något annat processteg, blev kvaliteten på kontaktytan bättre än om skalet togs bort i två separata steg. En annan slutsats från projektet var att även vatten kan användas för att ta bort GaSb, vilket är positivt eftersom det är en renare, billigare och enklare process än att använda MF319.

Cooperpar uppstår i supraledande material vid väldigt låga temperaturer. Detta är anledningen till varför de elektriska mätningarna i detta examensarbete utfördes i en anordning som håller temperaturen vid 50 mK, vilket är mer än 1000 gånger kallare än rumstemperatur. Om det upptäcks en strömökning i de två normala kontakterna när det går en ström samtidigt genom båda kvantprickarna, kan detta bero på att elektronerna i Cooparparet har delats upp och separerats till varsin kvantprick. En sådan signal kan dock vara väldigt svag och svår att upptäcka på grund av brus. I detta projekt har därför olika mätmetoder, som antingen använder likström eller växelström, jämförts, för att ta reda på vilken mätmetod som är mest lämpliga att använda.

En viktig upptäckt i detta arbete var att påvisa risken för falska signaler som kan uppstå under likströmsmätningarna men som inte beror på att elektronerna i ett Cooperpar har delats upp. Dessa signaler kan uppstå på grund av en spänningsskillnad mellan olika komponenter i kretsen som bidrar till att strömmen genom en av kvantprickarna påverkar strömmen genom den andra kvantpricken. Någon signal som skulle tyda på en uppdelning av elektronerna i ett Cooperpar kunde dock inte ses. Anledningen till detta är troligtvis att avståndet mellan kvantprickarna i nanotråden var för stort, eftersom elektronerna förlorar sin sammanflätning med varandra efter en tid.

# Abbreviations

| | |
|---|---|
| AC | Alternating current |
| Al | Aluminum |
| Au | Gold |
| BCS | Bardeen-Cooper-Schrieffer |
| CAR | Crossed Andreev reflection |
| CI | Constant interaction |
| CPS | Cooper pair splitting |
| DC | Direct current |
| EBL | Electron beam lithography |
| EPR | Einstein-Podolsky-Rosen |
| FWHM | Full-width at half-maximum |
| GaSb | Gallium antimonide |
| $H_2O$ | Water |
| HCl | Hydrochloric acid |
| IPA | Isopropanol |
| InAs | Indium arsenide |
| LPT | Local pair tunneling |
| MIBK | Methyl-isobutyl-ketone |
| N | Normal conductor |
| $N_2$ | Nitrogen gas |
| Ni | Nickel |
| PMMA | Polymethyl methacrylate |
| QD | Quantum dot |
| S | Superconductor |
| SEM | Scanning electron microscope |
| Si | Silicon |
| $SiO_2$ | Silicon dioxide |
| SPT | Shiba-assisted local pair tunneling |
| TMAH | Tetramethylammonium hydroxide |
| Ti | Titanium |
| WZ | Wurtzite |
| YSR | Yu-Shiba-Rusinov |
| ZB | Zinc blende |

# Symbols

| | |
|---|---|
| $\alpha_{bg}$ | Back gate lever arm |
| $B_{\|\|}$ | Magnetic field parallel to the substrate surface |
| $\Delta$ | Superconducting gap |
| $\Delta\mu$ | Difference in chemical potential between S and N |
| $\delta\varepsilon$ | Single-particle energy level spacing |
| $\delta r$ | Separation distance between electrons of a Cooper pair |
| $\varepsilon$ | Single-particle energy level |
| $e$ | Elementary charge |
| $E$ | Energy |
| $E_{add}$ | Additional energy |
| $E_C$ | Charging energy |
| $\Gamma_N$ | Coupling between normal lead and quantum dots |
| $\Gamma_S$ | Coupling between superconductor and quantum dots |
| $G$ | Conductance |
| $g^*$ | Effective $g$-factor |
| $h$ | Planck constant |
| $\hbar$ | Reduced Planck constant |
| $I_{1,2}$ | Current through quantum dots |
| $I_{sd}$ | Source-drain current |
| $k_B$ | Boltzmann constant |
| $\mu_B$ | Bohr magneton |
| $\mu_N$ | Chemical potential of normal leads |
| $\mu_S$ | Chemical potential of superconducting lead |
| $\mu_{QD}$ | Chemical potential of quantum dots |
| $T$ | Electron temperature |
| $T_c$ | Critical temperature |
| $\xi, \xi_0$ | Coherence length |
| $V_{AC}$, $V_{rms}$ | Root-mean-square voltage |
| $V_{bg}$ | Back gate voltage |
| $V_{sd}$ | Source-drain voltage |

# Contents

# Chapter 1

# Introduction

## 1.1 Background

Every wave function can be represented as a superposition of several eigenstates. According to the Copenhagen interpretation of quantum mechanics, the wave function collapses to a single eigenstate upon measurement when the wave function interacts with the external world. Prior to the measurement, the wave function involves all the various probabilities for the different eigenstates. Therefore, in this interpretation, the system is unknown until the measurement.

The year was 1935 when an article was published that would start a debate in the community of quantum physics. The authors of the acclaimed article [1] were the three physicists, Albert Einstein, Boris Podolsky, and Nathan Rosen, who together formed the trio EPR. The article presented a thought experiment that later became known as the EPR paradox. The authors considered two spatially separated entangled particles such that a measurement on one of the two particles immediately would determine the state of the other particle. EPR, however, argued that a measurement on one of the particles could not instantaneously affect the other particle since this would violate the rule of special relativity, stating that no physical object, message, or field can travel faster than the speed of light. This would show that the Copenhagen interpretation of quantum mechanics was not a complete description of the physical reality. EPR meant instead that the superposition of the state reflects our lack of knowledge about the particle and that the state of the second particle in fact must be determined before the measurement on the first particle, even from the moment of their creation. This lack of knowledge was explained as local hidden variables in both particles, which carried all information. Therefore, no information needed to travel from one particle to the other at the time of the measurement, and no rule of special relativity needed to be broken.

The hidden-variable theory was a valid alternative to quantum mechanics for almost 30 years, but in 1964 the physicist John S. Bell published a paper [2] in which he formulated the hidden-variable theory mathematically and arrived at a result that today is known as Bell's inequality. The inequality holds with the results one would expect in a deterministic reality where a measurement on one of the entangled particles will be unaffected by operations on the other particle, but the inequality was shown to be incompatible with the statistical predictions of quantum mechanics. Bell's inequality is experimentally testable [3] and has, for example, been violated with pairwise entangled photons separated by more than 10 km [4]. Quantum entanglement between two particles is a fundamental resource for quantum information technologies [5] and opens the door to many new possibilities within dense coding [6], quantum teleportation [7], and entanglement-based quantum cryptography [8].

Quantum entanglement also exists in superconducting solid state systems. A conventional superconductor can be used as a source of entangled electrons, because pairs of spin-singlet entangled electrons, called Cooper pairs, are formed in a superconductor according to the Bardeen-Cooper-Schrieffer (BCS) theory. CPS is a process in which the two spin-entangled electrons of a Cooper pair are split into two spatially separated electrons. CPS can occur in the structure illustrated in Figure 1.1a, where the two electrons of a Cooper pair in a superconducting contact, S, are separated into two different normal conductors, N1 and N2, via the quantum dots, QD1 and QD2.

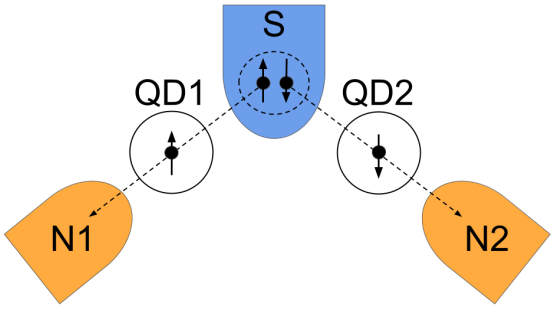


(a) Superconducting contact, S, quantum dots, QD1 and QD2, and normal conducting contacts, N1 and N2. The dashed circle indicates that the two electrons form a Cooper pair.

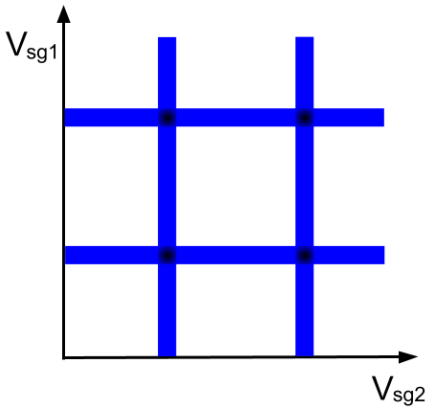


(b) Experimental signatures of CPS are pronounced peaks in the current when both quantum dots are in resonance.

Figure 1.1

CPS is often detected in experiments as spatial current correlations [9]. If the current through QD1 and QD2 is recorded simultaneously and plotted as a function of the side gate voltages, $V_{sg1}$ and $V_{sg2}$, controlling each quantum dot, these current correlations can manifest themselves as pronounced peaks when both quantum dots are in resonance. CPS is, therefore, a non-local signal i.e., the current in one of the normal contacts is affected by the side gate associated with the other normal contact. In Figure 1.1b the current through each quantum dot has been added and can be seen plotted as a function of $V_{sg1}$ and $V_{sg2}$. The blue lines show the current along resonant lines in the quantum dots and the black color indicates a higher current.

CPS has, for example, been demonstrated in experiments based on carbon nanotube devices [10], where a superconductor was coupled to two parallel quantum dots, and in semiconductor nanowires, where the two quantum dots were defined by two individual top gates [11], and by bottom gates [12].

One application of CPS devices is that they can serve as sources of spatially separated entangled electrons [13] [14]. Studying CPS can also be seen as a fundamental route for the exploration of the quantum mechanical property of non-locality and to detect electron entanglement by violating Bell's inequality in solid state systems [11]. This requires a deep understanding of the competing transport processes that can occur in a Cooper pair splitter and high efficiency of the desired CPS process. Another application of CPS is a system based on CPS between two parallel nanowires [15]. Such systems have theoretically been predicted to generate so-called parafermions, which are a generalization of Majorana fermions [16], but are computationally more powerful since they allow a larger set of operations for quantum computation [17].

## 1.2 Objectives and research questions

The ultimate goal of this thesis was to detect Cooper pair splitting in indium arsenide (InAs) nanowires with crystal phase-defined quantum dots. The motivation for the project is that if CPS is possible in these nanowires, this can lead to spin-resolved CPS and a test of Bell's inequality in the future. Nanowires with crystal-phase defined quantum dots seem promising for this because, in these systems, it is possible to control the spin-ground state with small electric and magnetic fields [18]. In order for CPS to be detected in these nanowires, the superconductivity must be induced from the superconducting contact to a segment of InAs between the two quantum dots, via the proximity effect. This differs from other systems where CPS has been detected. Since CPS has not been detected in these nanowires before, there are many uncertainties and risks with this project. The ultimate goal turned out to be quite difficult to achieve, and there are still several topics to investigate further in order for this ultimate goal to be met.

One research question for this project was to compare two different processing schemes and find out which one gave the highest quality of the InAs-titanium/aluminum (Ti/Al) contact interface. Additional research topics were to compare three different etching methods and find out if $H_2O$ can be used as an etchant for gallium antimonide (GaSb).

Another research topic for this thesis was to compare an AC measurement technique using a lock-in amplifier with a standard DC measurement technique and answer the question of whether it is necessary to use the AC technique for detecting CPS.

A final research topic was to discuss how suitable the design of the quantum dots was and how realistic it is to create a Cooper pair splitter device based on nanowires with crystal-phase defined quantum dots.

## 1.3 Outline

This thesis is organized as follows:

Chapter 2 covers the relevant theory needed for this thesis. The chapter is divided into four sections. The first section is about the electron transport of quantum dots. Above all, the section describes how quantum dots can be characterized. The second section is about superconductivity, especially the BCS theory and the transport that takes place between normal-superconductor interfaces. The third section presents the theory of a Cooper pair splitter device and contains a discussion of a regime of interest, describing what system parameters should be used for ideal Cooper pair splitting. In the last section a short description of Yu-Shiba-Rusinov (YSR) states is presented.

Chapter 3 describes the design and fabrication of Cooper pair splitter devices using two different processing schemes. The comparison between these two processing schemes was performed by electrical measurements at room temperature. The results from these measurements are also presented in this section. In addition, a number of studies were performed to compare GaSb etching using the developer MF319 and $H_2O$.

Chapter 4 is about the electrical measurements performed in a dilution refrigerator on one of the devices. Throughout the chapter, comparisons are made between AC and DC measurements. The quantum dots are characterized, and the results from Cooper pair splitting measurements are discussed on the basis of the regime of interest presented in Chapter 2.

Chapter 5 provides a short and concise summary of the whole thesis with an emphasis on the most important findings and future prospects.

# Chapter 2

# Theory

## 2.1 Quantum dots

Many topics of current research within solid state physics rely on the possibility of studying the physics of low-dimensional structures, namely structures where the degrees of freedom are restricted in one, two, or three spatial dimensions. Such structures are generally referred to as quantum wells, quantum wires, and quantum dots (QDs). If a quantum dot is coupled to electrical leads through tunnel junctions, the energy spectrum of the quantum dot can be probed by charge transport measurements at low temperatures.

### 2.1.1 Constant interaction model

A common way to describe electron transport through quantum dots is via the constant interaction model (CI), first presented by Beenakker in 1991 [19]. A schematic illustration and the circuit equivalent of the quantum dot used in the CI model can be seen in Figure 2.1. The quantum dot is tunnel-coupled to the source and drain with capacitances $C_s$ and $C_d$ and resistances $R_s$ and $R_d$. The quantum dot is capacitively coupled to the side gate electrode with capacitance $C_{sg}$ and to the back gate electrode with capacitance $C_{bg}$.

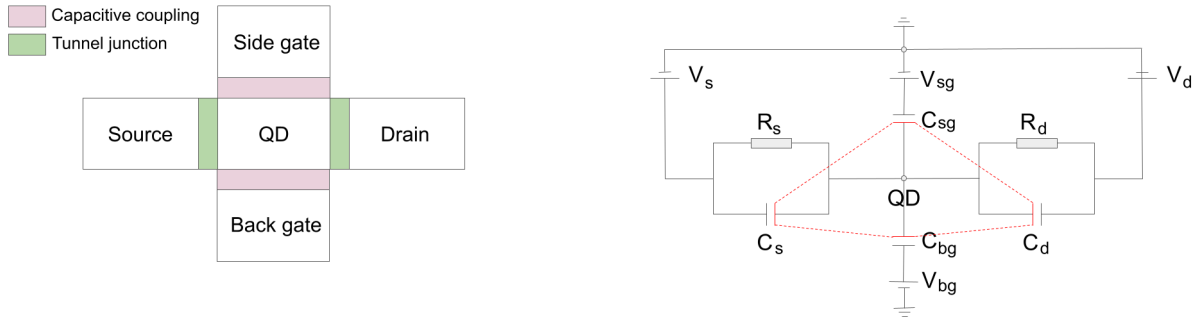


(a) Schematic illustration of a quantum dot tunnel-coupled to source and drain contacts and capacitively coupled to side gate and back gate contacts.

(b) Circuit equivalent where $C_i, R_i$ and $V_i$ represent the capacitance, resistance, and voltages for $i = s, d, sg, bg$, i.e., the source, drain, side gate, and back gate.

Figure 2.1

Consider a system with $m$ electrodes connected to a quantum dot. Each electrode makes a contribution to the total charge of the quantum dot, $Q$, which can be calculated as,

$$Q = \sum_{j=0}^{m} C_j V_j, \tag{2.1}$$

where $C_j$ is the capacitance between the quantum dot and electrode $j$ (source $s$, drain $d$, side gate $sg$ and back gate $bg$), and $V_j$ is the electrostatic potential of electrode $j$. Index 0 corresponds to the charge contribution from the number of electrons on the quantum dot. For a quantum dot with $N$ electrons $C_0V_0 = eN$, where $e$ is the elementary charge. The total electrostatic potential of the quantum dot, $V$, can then be written as,

$$V = \frac{1}{C_\Sigma}\left(-eN - C_sV_s - C_dV_d - C_{sg}V_{sg} - C_{bg}V_{bg}\right), \tag{2.2}$$

where $C_\Sigma$ is the self-capacitance of the quantum dot. In order for charge neutrality to hold $C_\Sigma$ must be equal to $C_\Sigma = -(C_s + C_d + C_{sg} + C_{bg})$. The total electrostatic energy of the quantum dot at fixed gate voltages can therefore be written as,

$$U(N) = \int_0^{-eN} V dQ = \frac{e^2N^2}{2C_\Sigma} + eN\left(\sum_{j=1}^{m}\frac{C_jV_j}{C_\Sigma}\right). \tag{2.3}$$

The total energy of the quantum dot, $E(N)$, can be obtained by adding the discrete values of the single-particle energy, $\varepsilon_i$, due to quantum confinement,

$$E(N) = \sum_{i=1}^{N}\varepsilon_i + \frac{e^2N^2}{2C_\Sigma} + eN\left(\sum_{j=1}^{m}\frac{C_jV_j}{C_\Sigma}\right). \tag{2.4}$$

Within CI, it is assumed that the energy levels, $\varepsilon_i$, can be calculated from non-interacting electrons, i.e., independent of the number of electrons on the dot. These energy levels are sometimes called orbitals because of the resemblance of quantum dots to real atoms. The chemical potential, $\mu_N$, is defined as the change in the total energy of the quantum dot when adding the $N$th electron and can thus be written as,

$$\mu_N = E(N) - E(N-1) = \varepsilon_N + \frac{e^2}{C_\Sigma}\left(N - \frac{1}{2}\right) - e\sum_{j=1}^{m}\alpha_jV_j, \tag{2.5}$$

where $\alpha_j = \frac{C_j}{C_\Sigma}$ is called the lever arm of electrode $j$ to the quantum dot. Finally, the additional energy for adding the $N$th electron, $E_{add}$ can be determined, which is defined as changes in the chemical potential,

$$E_{add} = \Delta\mu_N = \mu_N - \mu_{N-1} = \varepsilon_N - \varepsilon_{N-1} + \frac{e^2}{C_\Sigma} = \delta\varepsilon + E_C, \tag{2.6}$$

where $E_C$ is called the charging energy and $\delta\varepsilon$ is the spacing of the single-particle energy levels. By looking at (2.6) it can be seen that there are two contributions to the energy quantization in quantum dots. First, the spacing of the single-particle energy levels due to quantum confinement, and second, the charging energy due to the quantized nature of the electron charge together with the Coulomb interaction between electrons.

Equation (2.6) may describe a "ladder" of electrochemical potential, which is illustrated in Figure 2.2 and represents a quantum dot tunnel-coupled to metallic source and drain electrodes. The particular example in the figure shows no sign of quantum confinement since all levels are equally spaced. A small source-drain voltage, $V_{sd} = V_s - V_d$ has been applied over the leads. At low temperatures, all available electron states up to the chemical potential of the source and drain, $\mu_s$ and $\mu_d$, will be filled with electrons. An electron can only enter the quantum dot if there is an energy level between $\mu_s$ and $\mu_d$, i.e., if the quantum dot has an

energy level in the source-drain bias window. In Figure 2.2a, the electrochemical potential $\mu_N$ is above the lead potentials and the lead electrons do not have enough energy to enter the energy level $E(N)$. The figure also shows that $\mu_{N-1} < \mu_s$ and $\mu_{N-1} < \mu_d$. This means that there are no available states in the Fermi leads that the electron on energy level $E(N-1)$ can occupy. Therefore, the number of electrons is fixed and the quantum dot is said to be in the Coulomb blockade regime.

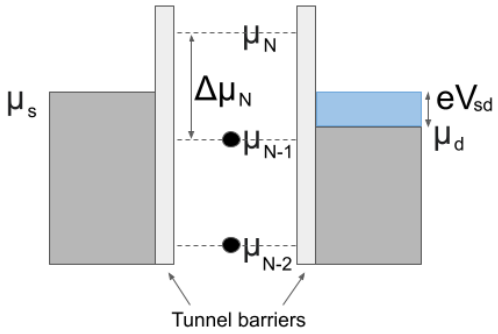


(a) Coulomb blockade regime, where no energy level on the quantum dot is within the bias window, and no current can be flown.

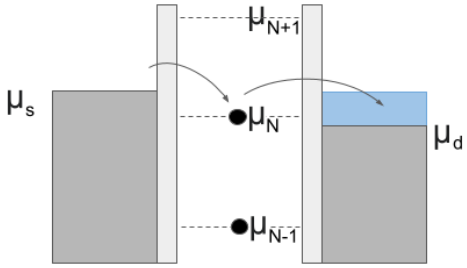


(b) One energy level within the bias window. The electron can now tunnel through the quantum dot giving rise to a source-drain current.

Figure 2.2: Quantum dot tunnel-coupled to source and drain electrodes with chemical potentials of $\mu_s$ and $\mu_d$, respectively. The additional energy to add the $N$th electron to the dot is denoted $\Delta\mu_N$. The blue part is the difference between $\mu_s$ and $\mu_d$ and is set by the small applied bias $eV_{sd}$ and is called the bias window.

From equation (2.5) it can be seen that the energy levels on the quantum dot depend linearly on the gate voltages as $-e\alpha_{sg}V_{sg}$ and $-e\alpha_{bg}V_{bg}$. By increasing $V_{sg}$ and $V_{bg}$, $\mu_N$ will decrease and eventually be inside the bias window. This situation is illustrated in Figure 2.2b. Since $\mu_d < \mu_N$, there are available states in the drain lead to which the electron on energy level $E(N)$ can tunnel. At the same time $\mu_s > \mu_N$, and a new electron can tunnel into the quantum dot. The limit when sequential tunneling can occur is when the three levels are all in resonance, i.e., $\mu_s = \mu_N = \mu_d$. The sequential tunneling of electrons will result in an oscillating source-drain current $I_{sd}$. The conductance, $G = \frac{I_{sd}}{V_{sd}}$, measured as a function of the back gate voltage $V_{bg}$ is usually referred to as Coulomb oscillations, where peaks can be observed when the quantum dot is resonant. The distance between the peaks is given by $\frac{E_{add}}{\alpha_{bg}}$. A calculation of Coulomb oscillations can be seen in Figure 2.3.

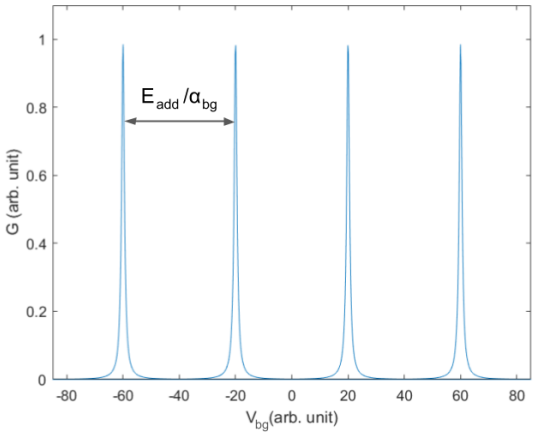


Figure 2.3: Calculated Coulomb oscillations. The distance between the peaks is given by $\frac{E_{add}}{\alpha_{bg}}$.

### 2.1.2 Line shape of the conductance peaks

This section, which will discuss the line shape of the conductance peaks in Coulomb oscillations, is based on Ref. [19]. Note that this theory is built upon linear-response, and the equations given for the conductances will only be true in the limit of vanishingly small source-drain voltages.

To distinguish two limiting regimes, one can use the coupling of a level $\Gamma = \Gamma_s + \Gamma_d$, where $\Gamma_s$ and $\Gamma_d$ are called the couplings to the source and the drain, respectively. In this thesis the couplings have the unit energy. The two regimes are called the weak-coupling regime where $\Gamma \ll k_B T$ and the strong-coupling regime where $\Gamma \gg k_B T$. $k_B$ is the Boltzmann constant and $T$ is the electron temperature. The main assumption in the weak-coupling regime, $\Gamma \ll k_B T$, is that the conductance peaks are thermally broadened. A theoretical model for this regime was first presented by Beenakker in 1991 [19]. The charge is assumed to be well defined, which means that the probability of finding an electron on the dot is either one or zero. This is equivalent to saying that only first-order tunneling processes are allowed and higher-order tunneling via virtual intermediate states can be neglected. [20] The single level contribution to the conductance of the $i$'th Coulomb peak, $G_i$, is given by,

$$G_i = \frac{e^2}{4k_b T}\left(\frac{1}{\Gamma_i^s} + \frac{1}{\Gamma_i^d}\right)^{-1} \cosh^{-2}\left(\frac{\alpha_{bg}(V_{bgi}^{max} - V_{bg})}{2k_B T}\right) = G_i^{max} \cosh^{-2}\left(\frac{\alpha_{bg}(V_{bgi}^{max} - V_{bg})}{2k_B T}\right). \tag{2.7}$$

where $V_{bgi}^{max}$ is the position of the peak, $\Gamma_i^s$ is the coupling to the source, $\Gamma_i^d$ is the coupling to the drain, and $G_i^{max}$ is the maximum conductance. Since the amplitude of the peaks depend on the orbital, a pairwise behavior should be observed for spin degenerate systems.

In the strong-coupling regime, where $\Gamma \gg k_B T$, the shape of a single resonant level is approximately given by a Lorentzian function [21]

$$G_i = \frac{4\Gamma_i^s \Gamma_i^d}{(\Gamma_i^s + \Gamma_i^d)^2}\frac{e^2}{h}\frac{\Gamma_i^2}{4(\alpha_{bg}(V_{bgi}^{max} - V_{bg})^2 + \Gamma_i^2} = G_i^{max}\frac{\Gamma_i^2}{4(\alpha_{bg}(V_{bgi}^{max} - V_{bg})^2 + \Gamma_i^2}, \tag{2.8}$$

where $\Gamma_i = \Gamma_i^s + \Gamma_i^d$ and $h$ is the Planck constant. In this regime, tunneling does not need to be sequential and higher order processes become important. The details of this model are outside the scope of this thesis. The full-width at half-maximum (FWHM) is given by $\Gamma$. In Figure 2.4 a conductance peak has been plotted in the weak-coupling regime with $k_B T = 0.3$ and in the strong-coupling regime with $\Gamma = 1.0$.

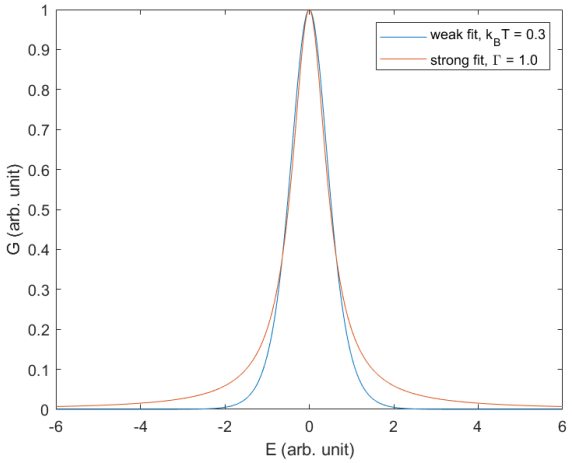


Figure 2.4: Coulomb peak in the weak-coupling regime and in the strong-coupling regime. Conductance, $G$, as a function of energy, $E$.

### 2.1.3 Charge stability diagram

Parameters such as the charging energy $E_C$, the level spacing $\delta E$ and the back gate lever arm $\alpha_{bg}$ can be extracted from a so-called charge stability diagram, where the current, $I_{sd}$, or the differential conductance, $\frac{dI_{sd}}{dV_{sd}}$, is plotted as a function of both source-drain bias $V_{sd}$ and back gate voltage $V_{bg}$. An illustration of such a two-dimensional diagram can be seen in Figure 2.5.

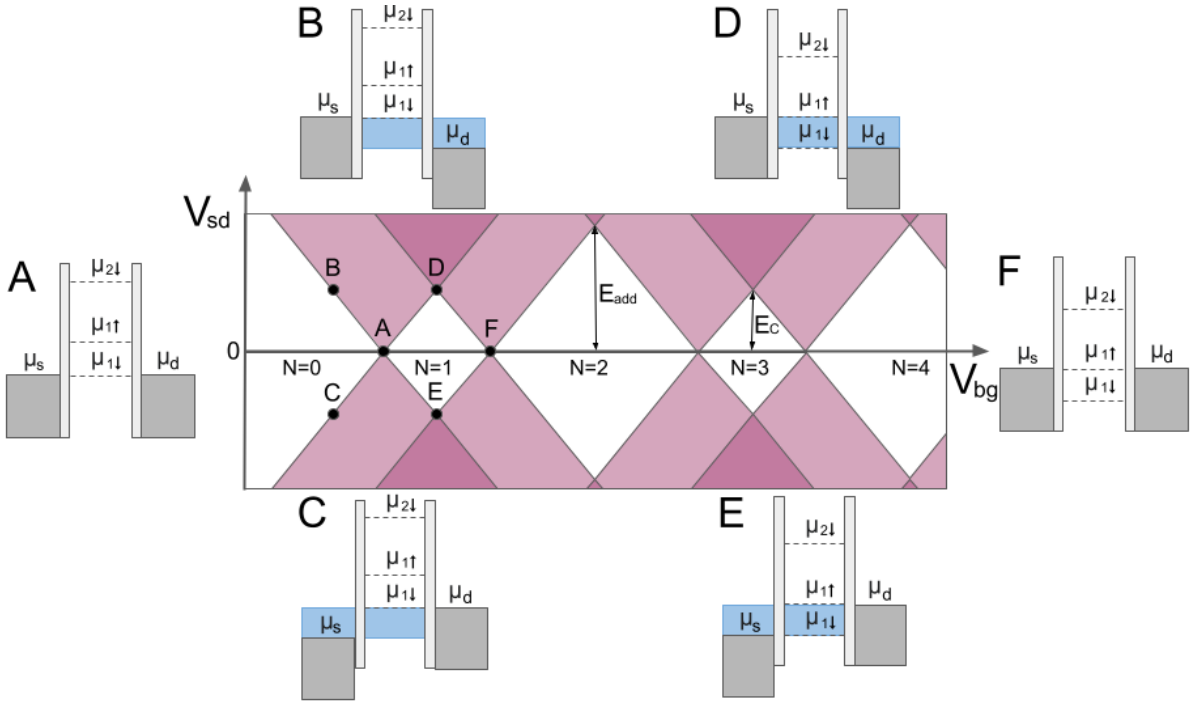


Figure 2.5: Schematic illustration of a charge stability diagram. The current, $I_{sd}$, is plotted as a function of source-drain voltage, $V_{sd}$, and back gate voltage, $V_{bg}$. Within the white Coulomb diamonds, the system is in the Coulomb blockade regime where the number of electrons in the quantum dot, $N$, is fixed and no current flows. Diagrams of the electrochemical potential at points (A-F) are also illustrated. Note that $\mu_{1\downarrow}$ and $\mu_{1\uparrow}$ correspond to the same single-particle energy level, but to electrons with opposite spin.

Five white diamonds can be seen in the figure. These are called Coulomb diamonds and correspond to regions where no single-electron tunnel processes are allowed. Here prevails Coulomb blockade and the electron occupation, $N$, in the quantum dot is fixed. This has given the diagram its name since the charge is constant inside the diamonds. Outside the diamonds, the Coulomb blockade is lifted, and at least one state lies within the bias window. The black "V"-shaped lines correspond to transitions via a state in the quantum dot. If the slope on a line is negative, it means that the electrochemical potential of the specific state in the quantum dot is aligned with $\mu_s$, and if a line has a positive slope, it indicates that the electrochemical potential of the state is aligned with $\mu_d$. Below is a description, including the electrochemical-potential alignment of six different points in the stability diagram. Transport via excited states and second-order tunneling has not been included in the discussion.

At low back gate voltages, there is a large, non-closing Coulomb diamond. This diamond indicates that the quantum dot is completely depleted of electrons, i.e., $N = 0$. The states $\mu_{1\downarrow}$ and $\mu_{1\uparrow}$ correspond to the same single-particle energy level, but the states can hold electrons with opposite spin. At point A, when no source-drain voltage is applied, the back gate voltage has increased so much that the electrochemical potential at the lowest state in the quantum dot, $\mu_{1\downarrow}$, is aligned with $\mu_s$ and $\mu_d$. Two black "V"-shaped lines originate from point A. These lines define the boundaries of the adjacent diamonds and are associated with the onset of transport of a first electron in the quantum dot. In point B, $\mu_{1\downarrow}$ is aligned with $\mu_s$, and in point C, $\mu_{1\downarrow}$ is aligned with $\mu_d$. In point D, $\mu_{1\downarrow}$ is aligned with $\mu_d$, and the second-lowest state in the quantum dot, $\mu_{1\uparrow}$, is aligned with $\mu_s$, while the opposite is true in point E.

In the light pink areas, there is only one state within the bias window and only transport of single-electron type is allowed, meaning that only one electron can tunnel through the quantum dot at a time. In the dark pink areas, two-electron transport is allowed. Since there are two states, separated by the charging energy, within the bias window, it is possible for two electrons to tunnel into the dot before one electron tunnels out.

At point F, the back gate voltage has increased further while the source-drain voltage is zero. At this point, $\mu_{1\uparrow}$ is aligned with $\mu_s$ and $\mu_d$. Two black lines originate from point F. These lines define the boundaries of the adjacent diamonds and are associated with the onset of transport of a second electron in the quantum dot. This second electron involves the same single-particle energy level as the electron in point A but has the opposite spin. The pattern of small and large Coulomb diamonds is typical of systems where the charging energy $E_C$ is comparable to the level spacing $\delta E$, i.e., for spin-degenerate systems. If all diamonds are of equal size, this instead indicates $E_C \gg \delta\varepsilon$, which is typical for semiconductor quantum dots in the many-electron regime.

The additional energy, $E_{add}$, can be extracted from the charge stability diagram as the height of the large diamonds,

$$E_{add} = \text{ height of a large diamond,} \tag{2.9}$$

while the height of the smaller diamonds gives the charging energy,

$$E_C = \text{ height of a small diamond.} \tag{2.10}$$

Under the assumption that $E_C$ is constant within an orbital, $\delta\varepsilon$ can be estimated as $E_{add} - E_C$. As can be seen in Figure 2.5 the diamonds are symmetric. According to Ref. [22] this is typical for back-gated quantum dots in nanowires since the source and drain capacitances often are similar in magnitude and larger than the back gate capacitance. If $C_s \sim C_d > C_{bg}$, the back gate lever arm $\alpha_{bg}$ can be determined from the ratio of the height $\Delta V_{sd}$ and width $\Delta V_{bg} = \frac{e}{C_g}$ of the small diamonds,

$$\alpha_{bg} = \frac{\Delta V_{sd}}{\Delta V_{bg}} = \frac{\text{height of a small diamond}}{\text{width of a small diamond}}. \tag{2.11}$$

## 2.2 Superconductivity

This section will cover a brief description of the phenomenon of superconductivity with key components which are of importance for this thesis. For a more detailed description, the reader is referred to Refs. [23] [24].

Heike Kamerlingh Onnes made the first observation of superconductivity in 1911. During transport measurements on mercury, he realized that the electrical resistance vanished below a certain critical temperature, $T_c$. [25]. Superconductivity exists for some metals and compounds, with two distinguishable features. The existence of zero-resistance, which allows for dissipationless currents, is one of the features. The other feature is that superconductors are perfect diamagnets, which means that the interior of a superconductor is completely shielded from external magnetic fields. The second feature was discovered by Meissner and Ochsenfeld in 1933 [26]. At a certain critical magnetic field, $B_c$, the superconductivity breaks down due to the energy costs to repel the magnetic field from the interior of the superconductor. When the temperature rises above $T_c$ or the magnetic field becomes larger than $B_c$, the superconductivity is quenched, and the material transitions to its normal state.

### 2.2.1 BCS theory

The first model that could combine the macroscopic properties of superconductors with microscopic quantum mechanics was the Bardeen-Cooper-Schrieffer (BCS) theory presented in 1957 [27]. What is especially important in the BCS theory is that electrons with opposite momenta and opposite spin can pair up and form Cooper pairs due to a net attractive interaction mediated by phonons in the crystal lattice [28]. Only s-wave superconductors will be considered in this thesis since both superconductors used, aluminum and titanium, are s-wave superconductors. The wave function for a superconductor has both a spin and an orbital component. For s-wave superconductors, the spin component is a singlet state, meaning that the electrons have opposite spin with total spin angular momentum $S = 0$. The orbital part has angular momentum $l = 0$, which is called the s-orbital, hence the name s-wave superconductors.

Due to the pairing process, there will be an energy gap in the quasiparticle density of state, $N_S$, around the Fermi energy, $E_F$, with size $2\Delta$. $\Delta$ is the minimum energy required to break a Cooper pair, and will in this thesis be referred to as the superconducting gap. The energy $2\Delta$ can be seen as the excitation energy of the two electrons which result from breaking up a Cooper pair. These excitations are called Bogoliubov quasiparticles and behave similarly to electrons and holes in a normal metal far away from the Fermi energy. This means that the quasiparticle density of states looks similar to the normal density of states, $N_N$, far away from the Fermi level. However, close to the Fermi energy, the quasiparticles start to behave differently due to the pairing process. The quasiparticle density of states can be written as,

$$\frac{N_S(E)}{N_N(E_F)} = \begin{cases} \frac{|E-E_F|}{\sqrt{((E-E_F)^2)-\Delta^2}}, & \text{for } |E-E_F| > \Delta \\ 0, & \text{for } |E-E_F| < \Delta. \end{cases} \tag{2.12}$$

The equation shows that there are no quasiparticle states for $|E-E_F| < \Delta$ in the gap. Also, when $|E-E_F| = \Delta$, $N_S$ diverges. The BCS theory predicts a relationship between the size of the gap and the critical temperature as,

$$\Delta(T=0) = 1.764 k_B T_c. \tag{2.13}$$

The gap shrinks with increasing temperatures and increasing applied magnetic field until it finally disappears at $T = T_c$ or $B = B_c$. This behavior of superconductors is often used to perform control measurements in the normal conducting state. In this thesis, the control measurements will be performed by increasing the magnetic field above $B_c$.

### 2.2.2 Proximity effect

The Cooper pairs do not abruptly disappear at a normal conductor-superconductor (N-S) interface, but rather decays smoothly. This property of superconductivity has an interesting consequence, namely the proximity effect, which allows Cooper pairs to leak into a normal conducting material and leads to superconducting behavior in the proximitized material. For example, if a quantum dot is electrically connected to one normal drain contact and one superconducting source contact, the divergence in the quasiparticle density of states, described by Equation (2.12), will give rise to distinct peaks in the charge stability diagram for $V_{sd} = \pm\frac{\Delta}{e}$. This is illustrated in Figure 2.6. Note that the figure only shows a rough sketch of the approximate appearance. In reality, it looks different. The purpose of the figure is to show that the superconductivity will give rise to a gap around $V_{sd} = 0$ during measurements of charge stability diagrams. Even though a more detailed theory behind the superconducting gap is beyond the scope of this thesis, the appearance of the superconducting gap is a distinct characteristic of superconductivity and will be used as such in this thesis.

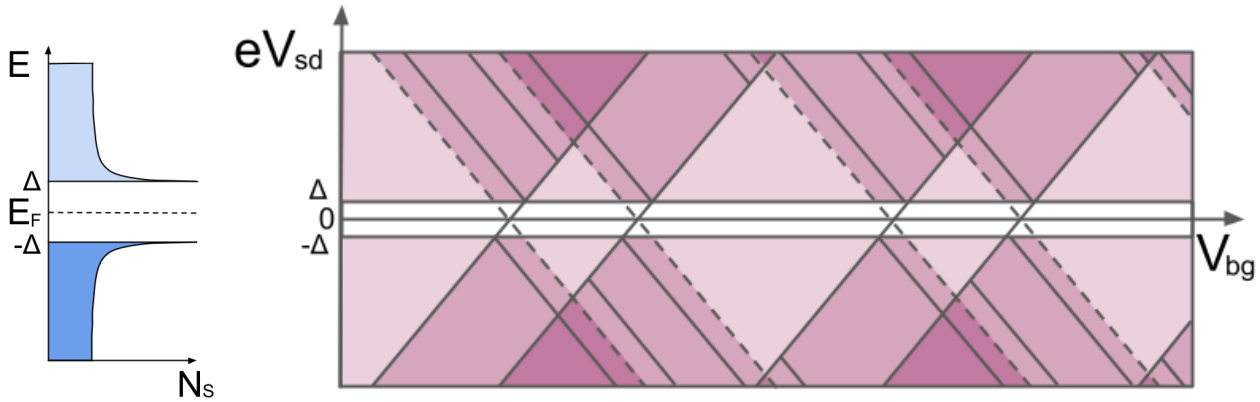


(a) (b)

Figure 2.6: a): Superconducting gap around the Fermi energy in the quasiparticle density of states, $N_S$ b): Superconducting gap of size $\Delta$ in a charge stability diagram. Note that the figure only shows a rough sketch of the approximate appearance. In reality, it looks different.

The proximity effect is carried out by a process called Andreev reflection. If an electron with sub-gap energy, $|E| < \Delta$, is approaching S from N, it can not simply enter S since it is forbidden to enter the superconducting gap where only Cooper pairs exist. Instead, the electron pairs up with an electron with opposite spin and momentum and enters S as a Cooper pair. The second electron leaves a hole in N. This hole will retrace the path of the incident electron in a process known as retro-reflection. The same process but time-reversed happens when a hole is approaching S from N. The hole will be retro-reflected as an electron with opposite spin and corresponds to a Cooper pair leaking from S into N, which gives rise to the proximity effect. The Andreev process and the time-reversal process are illustrated in Figures 2.7a and 2.7b. It is also possible for a hole entering S at position $x$, to be retro-reflected as an electron a distance $L$ away from $x$ if $L < \xi_0$, where $\xi_0$ is the coherence length of the superconductor, i.e. the average distance which an electron travels before it loses its entanglement with the other electron. This enables a Cooper pair to split into two separated normal contacts, denoted N1 and N2, and can serve as a source of spin-entangled electrons. This process is known as crossed Andreev reflection (CAR) and is depicted in Figure 2.7c where an incoming hole from N1 is reflected as an electron into N2, which corresponds to CPS into two separate leads.

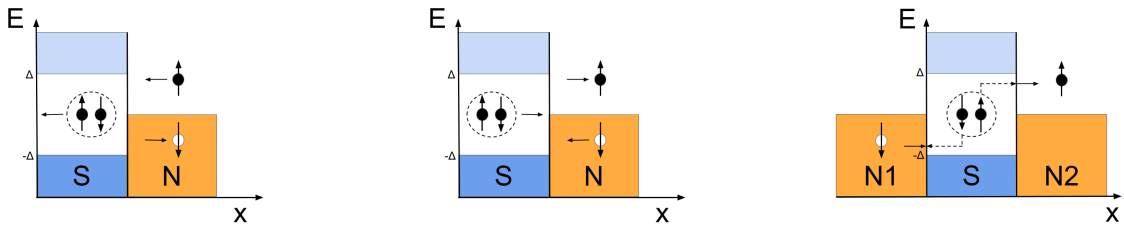


(a) Andreev reflection process. An incoming electron from N to S creates a Cooper pair in S and leaves a retro-reflected hole in N.

(b) Time-reversal Andreev reflection process. An outcoming electron from S to N removes a Cooper pair in S and leaves a retro-reflected hole in N.

(c) Crossed Andreev reflection. An incoming hole from N1 is reflected as an electron into N2 and a Cooper pair is removed from S.

Figure 2.7

## 2.3 Cooper pair splitter

In Section 2.2.2, the mechanism CAR was presented, which describes how the electrons in a Cooper pair can be split into two different normal conductors. Ref. [13] proposes to use quantum dots to get an enhanced control of the CPS process. Consider the system presented in Figure 2.8 of a superconductor denoted S with a superconducting gap $\Delta$ and chemical potential $\mu_S$. $\delta r$ represents the separation distance between the electrons of a Cooper pair. The superconductor is coupled by tunneling barriers to two separate quantum dots, QD1 and QD2. The couplings between the superconductor and the quantum dots are denoted $\Gamma_{S1}$ and $\Gamma_{S2}$. The two quantum dots are coupled by tunneling barriers to two Fermi leads, $N1$ and $N2$, both with the same chemical potential, $\mu_N = \mu_{N1} = \mu_{N2}$. The chemical potentials on the respective quantum dots are denoted $\mu_{QD1}$ and $\mu_{QD2}$. The corresponding couplings between dots and leads are denoted $\Gamma_{N1}$ and $\Gamma_{N2}$. Note that the inter-dot coupling $\Gamma_{12}$ is assumed to be negligible [1]. By means of external gate electrodes, the chemical potentials on the quantum dots can be tuned such that both quantum dots are in resonance with the superconducting contact, i.e., $\mu_{QD1} = \mu_{QD2} = \mu_S$. The two quantum dots have single-particle energy levels, $\varepsilon_1$ and $\varepsilon_2$, and charging energy $E_{C1}$ and $E_{C2}$.

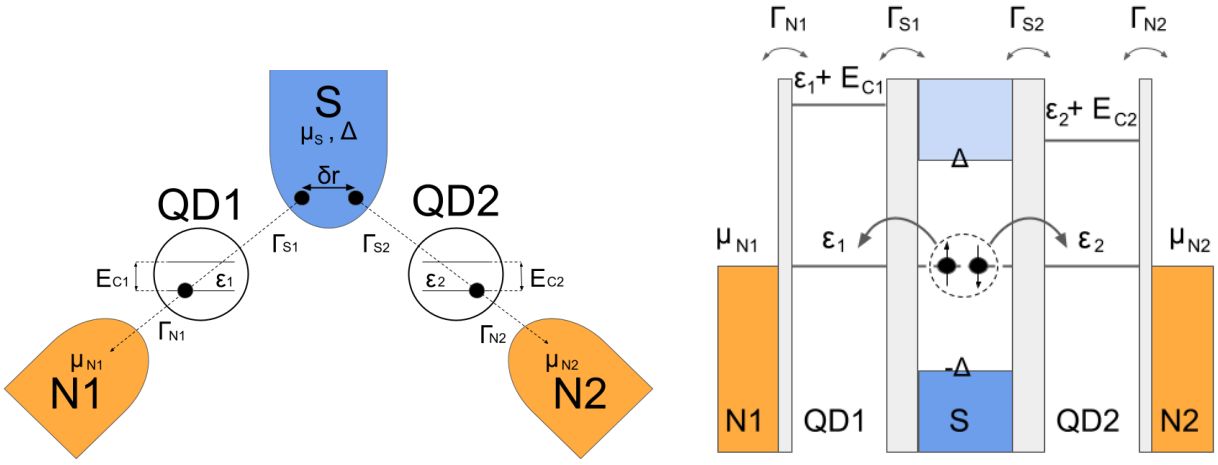


(a) CPS in real space. Figure adapted from [13][29].

(b) CPS in energy-space. Figure adapted from [29].

Figure 2.8

[1] For the system in this thesis the distance between the quantum dots is $\sim 550$ nm and has been assumed to be large enough to neglect any coupling, $\Gamma_{12}$, between the dots. This may not be applicable to other systems.

Instead of CPS, it is also possible that the electrons instead tunnel to the same normal lead. These processes will be referred to as local pair tunneling (LPT) as in Ref. [29]. In order to increase the ratio of CPS to LPT, ideal system parameters should be used. These parameters can be summarized into a regime of interest which will be presented in this section. The derivation of the regime of interest closely follows the reasoning in Refs. [13] and [29]. For simplicity, the tunnel coupling between the superconductor and the dots and between the dots and the leads will be assumed to be equal, i.e., $\Gamma_S = \Gamma_{S1} = \Gamma_{S2}$ and $\Gamma_N = \Gamma_{N1} = \Gamma_{N2}$. In addition, it is also assumed that $E_{C1} = E_{C2} = E_C$ to further facilitate the discussion.

A Cooper pair splitter involves two main energy scales, the charging energy of the quantum dots and the superconducting gap of the superconducting contact. It is, therefore, necessary that the device operates at a temperature where these two energy scales are well resolved. This means that one condition for the regime of interest is,

$$k_B T < E_C, \Delta. \tag{2.14}$$

A bias voltage, $|eV_{sd}|$, between S and each of the normal leads N1 and N2, [13]

$$|eV_{sd}| = \Delta\mu = \mu_S - \mu_N > 0, \tag{2.15}$$

is applied to extract the electrons from the superconducting contact to the normal leads. This bias voltage must also be sufficiently small for the important energy scales to be resolved,

$$\Delta\mu < E_C, \Delta. \tag{2.16}$$

According to Ref. [13] there are two different LPT processes competing with the CPS process. These two processes referred to as process A, and process B are illustrated in Figure 2.9.

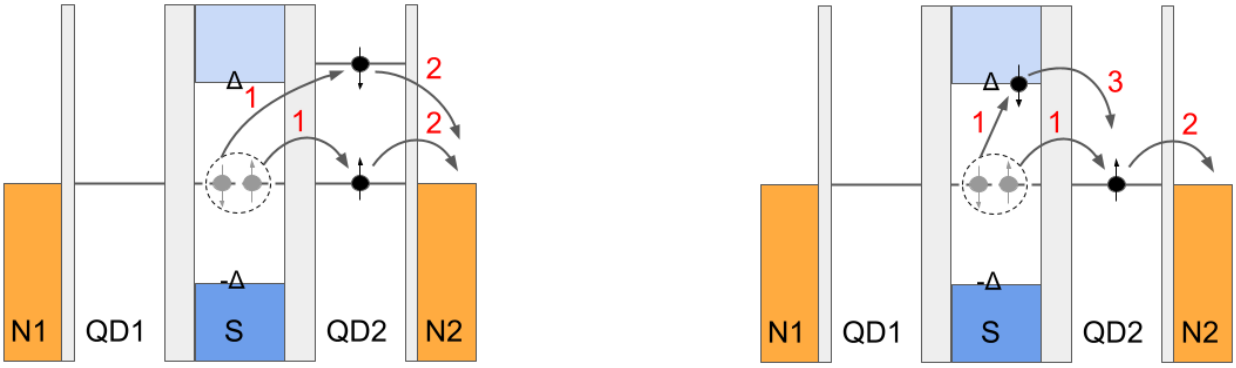


(a) LPT process A in energy-space.

(b) LPT process B in energy-space.

Figure 2.9: Local pair tunneling (LPT) processes competing with the desired CPS process. The red numbers refer to the different tunneling steps. Figure adapted from [29].

In process A, the two electrons of a Cooper pair tunnel simultaneously from S to one quantum dot before they tunnel to the normal lead. The red numbers in Figure 2.9a refer to these two tunneling steps. This process leads to a double occupancy of the dot and therefore requires a cost of the charging energy $E_C$. From the above equations (2.14) and (2.16) it can be seen that,

$$k_B T, \Delta\mu < E_C. \tag{2.17}$$

Process A is therefore suppressed by having sufficiently large charging energies. In process B, the two electrons of a Cooper pair tunnel sequentially through the same quantum dot. This transport process requires a virtual quasiparticle excitation. The first step in process B is that the Cooper pair is broken up, and one of the electrons tunnels to one of the quantum dots. In the meantime, the second electron waits in the superconductor in a virtual quasiparticle state. The second step is that the first electron tunnels to the normal lead, allowing the second electron to tunnel into the same quantum dot. The red numbers in Figure 2.9b refer to the different tunneling steps. The LPT process B, therefore, does not require any double occupancy of the quantum dots. The probability of this process increases with decreasing superconducting gaps. Equations (2.14) and (2.16) yield

$$k_B T, \Delta\mu < \Delta. \tag{2.18}$$

Process B can therefore be suppressed by having sufficiently large $\Delta$. The two LPT processes competing with CPS can be made arbitrarily small by increasing the charging energy $E_C$ and the size of the superconducting gap $\Delta$. At the same time, the desired CPS process requires neither a double occupancy of a quantum dot nor any virtual quasiparticle state and is therefore not negatively affected by having large $E_C$ or $\Delta$. This means that the ratio between the desired CPS process and the competing LPT processes theoretically can become arbitrarily small for $E_C, \Delta \to \infty$. [29] It is interesting to mention that the superconducting contact in this thesis was made of aluminum which has a rather small superconducting gap of about 180 µeV. The reason why aluminum was still chosen was because a small superconducting gap generally gives a longer coherence length $\xi_0$. This allows the electrons in the Cooper pair to travel longer distances from each other without losing their entanglement.

There are also other parameters that must be well-tuned for an ideal Cooper pair splitter. Ref. [13] suggests to work in a regime where,

$$\Gamma_N > \Gamma_S. \tag{2.19}$$

This asymmetric coupling would ensure that the electrons which enter the quantum dots will leave to the normal contacts much faster than new electrons can enter the dots from the superconductor. In this regime, the occupation probability on the quantum dots will, therefore, be very small. This facilitates the theoretical model since no concern must be taken regarding electrons that remain on the quantum dots, which otherwise could block subsequent CPS processes [29]. The occupation probability on the quantum dots will also be very small if [13]

$$\Delta\mu > k_B T, \tag{2.20}$$

which is a further requirement in the regime of interest. It is also desired to have quantum dots with a clear shell-filling pattern [29], which means that the energy level spacing $\delta\varepsilon$ is in the same order as the charging energy. If an electron tunnels from the superconducting contact into one of the quantum dots, it is possible that another electron with opposite spin leaves the dot and tunnels into the normal lead. This would result in loss of the entanglement, but such spin-flip processes can be avoided if

$$\delta\varepsilon > k_B T, \Delta\mu. \tag{2.21}$$

Another process that can lead to loss of entanglement is the occurrence of electron hole-pair excitations out of the Fermi sea of the leads. This means that the quantum dot levels can be filled by electrons from the Fermi leads. This would be unwanted since it would potentially exchange the entangled electron on the dot with an electron from the Fermi lead, which can happen if the couplings between the leads and the quantum dots are too strong. Ref. [13] argues that these processes will be suppressed if

$$\Gamma_N < \Delta\mu, \tag{2.22}$$

under the assumption that $\mu_N \approx \mu_S$. In this way, a large enough bias applied would make sure that the chemical potential of the Fermi leads, $\mu_N$ is well below the quantum dot resonances $\mu_{QD1}$ and $\mu_{QD2}$, which are controlled by the external gates.

By combining all equations from Section 2.3 a regime of interest for ideal Cooper pair splitting can be formulated, [13]

$$\begin{cases} \Delta, E_C, \delta\varepsilon > \Delta\mu > \Gamma_N, k_B T \\ \Gamma_N > \Gamma_S \end{cases} . \tag{2.23}$$

When studying Cooper pair splitting it is also important to consider the length scales in the devices. There are three length scales that have been considered especially important, namely:

1. The separation distance between the two electrons in the Cooper pair, denoted $\delta r$
2. The coherence length in the superconducting contact, denoted $\xi_0$
3. The coherence length in the semiconducting nanowire, denoted $\xi$.

However, these length scales are strongly influenced by which theoretical framework is chosen to best describe the experimental situation, but can be used as a rough guideline to determine how likely it is to detect Cooper pair splitting. The estimation of $\delta r$ can be given by the width of the superconducting contact [11] [29]. However, this is only an upper bound, since it is not possible to know the exact tunneling points of the electrons in the Cooper pair. For the CPS device in this thesis $\delta r = 400$ nm. In nanostructures made of diffusive thin films the coherence length can be expressed as

$$\xi \approx \sqrt{\frac{\hbar v_F l_{mfp}}{3\Delta}}, \tag{2.24}$$

in case of diffusive transport where $l_{mfp} < \xi$. $l_{mfp}$ is the mean free path of the electrons, $\hbar$ is the reduced Planck constant and $v_F$ is the Fermi velocity. The coherence length in these aluminum nanostructures, $\xi_0$, typically lie in the range of 100 to 200 nm [30]. Since the spin-entangled electrons in the Cooper pair must travel in both the superconducting contact and in the nanowire, it is also relevant to mention the coherence lengths for InAs nanowires. Note that the crystal structure probably affects the coherence length, but has not been studied further. In Ref. [31] the coherence length in diffusive InAs nanowires was estimated to $\xi = 250$ nm.

## 2.4 Yu-Shiba-Rusinov states

If a Cooper pair splitter operates in a regime with strong superconductor-dot coupling, Yu-Shiba-Rusinov (YSR) states can be formed, which will be briefly covered in this section, under the assumption that $\Gamma_N \ll \Gamma_S$. For a deeper theoretical description, the reader is referred to Ref. [32].

Since each single-particle energy level, $\varepsilon_i$, can hold two electrons of opposite spin, the quantum dot ground state generally changes between singlet and doublet as more electrons are put onto the quantum dot. A singlet state means that there are no unpaired electrons, while a doublet state means that there is one unpaired electron. YSR states can arise when the cost of breaking a Cooper pair is low compared to the cost of adding electrons to the dot i.e., $\Delta \ll E_C$. The formation of YSR states involves an interaction between the unpaired dot electron in the double state and a quasiparticle with opposite spin. The interaction forms bound states localized in the gap, singlet states composed of one dot-electron and one Bogoliubov quasiparticle. A common description is that the superconductor screens the spin of the quantum-dot with a quasiparticle from its bulk. YSR states can be seen in the charge stability diagram, as qualitatively sketched in Figure 2.10.

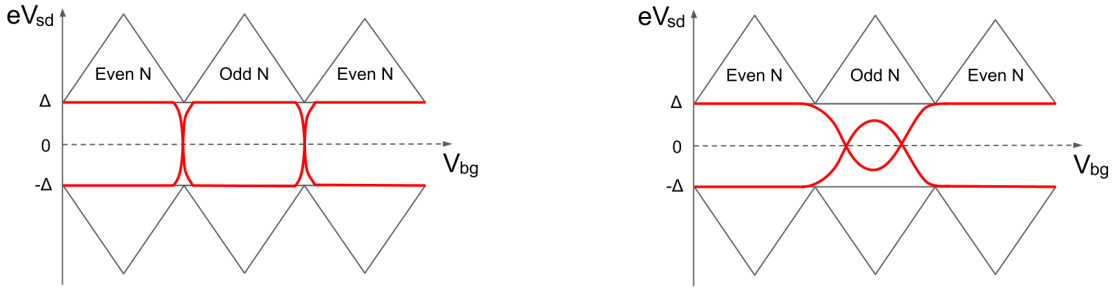


(a) (b)

Figure 2.10: Qualitative sketches of charge stability diagrams with YSR states. The black lines represent conventional Coulomb diamonds, while the red lines represent YSR states. $\frac{\Gamma_S}{E_C}$, is stronger in b) than in a). Note that the figure only shows a rough sketch of the approximate appearance of YSR states. In reality, it looks different. Figure adapted from [29].

When the source-drain voltage is higher than the superconducting gap, $|eV_{sd}| > \Delta$, conventional Coulomb diamonds can be seen. For simplicity, the diamonds have been drawn with equal sizes. YSR states can be seen within the superconducting gap for $|eV_{sd}| < \Delta$. For low $\Gamma_S$, the bound state is located near the edge of the gap, but the bound state moves down in energy towards the Fermi level as $\Gamma_S$ increases. In Figure 2.10b, the coupling to the superconductor relative to the charging energy, $\frac{\Gamma_S}{E_C}$, is stronger than in Figure 2.10a.

Non-local signals can also arise in a device even when there is no CPS if the coupling between the superconductor and the dot is sufficiently strong. The transport mechanism behind these non-local signals will be referred to as Shiba-assisted local pair tunneling (SPT) as in Ref. [9], because it involves the Yu-Shiba-Rusinov state, but result in the subsequent transitions of the two electrons in the Cooper pair into the same normal lead. It is important to know that if a non-local signal is detected, it may not solely be due to CPS, and more efforts are required to identify which part of the signal is caused by CPS. The purpose of this discussion is to mention one difficulty in detecting Cooper pair splitting that arises in a device with YSR states.

YSR states can be studied by means of a magnetic field [33], but when an external magnetic field is applied, the spin-degenerate orbital states split into two separate energy states due to the Zeeman effect. In the case of moderate B-fields, the energy separation between the two states, $\Delta E_Z$, can be calculated as,

$$\Delta E_Z = |g^*| \mu_B B, \tag{2.25}$$

where $B$ is the applied magnetic field, $g^*$ is the effective $g$-factor and, $\mu_B$ is the Bohr magneton.

# Chapter 3

# Processing

This chapter starts with an introduction to quantum dots in InAs nanowires defined with crystal-phase control. Then follows detailed descriptions of two different processing schemes for the fabrication of Cooper pair splitter devices. Electrical measurements on these devices were performed at room temperature and the results from these measurements are also presented. The purpose of these measurements was to find out which process gave the highest quality of the InAs-Ti/Al contact interface. The chapter ends with a series of etching studies performed to compare GaSb etching using MF319 and $H_2O$.

## 3.1 Crystal phase-defined quantum dots in InAs/GaSb core-shell nanowires

Quantum dots can be made in nanowires by inserting two closely spaced tunnel barriers in the axial direction. The quantum dots in this thesis were realized in InAs nanowires and defined by using two different crystal phases, zinc blende (ZB) and wurtzite (WZ). WZ InAs has up to 126 meV larger band gap than ZB InAs [34]. A simplified illustration of an InAs nanowire with WZ barriers and two ZB quantum dots is illustrated in Figure 3.1a. The conduction band edge $E_{CB}$ has also been drawn, where the WZ has been assumed to form a square potential barrier in the conduction band. The size of the quantum dots were approximately 10-20 nm and the size of the quantum dots together with the two barriers were approximately 60-70 nm. In the figure it can be seen that the two innermost barriers are thicker than the two outermost barriers. This is to meet the requirement that $\Gamma_N > \Gamma_S$ as presented in the regime of interest in Equation (2.23). The nanowires also had a shell of GaSb. Since WZ InAs has a relatively lower surface energy than InAS ZB, the radial growth of GaSb is suppressed [35]. Therefore, the nanowires will consist of InAs/GaSb core-shell segments that are separated by WZ InAs segments. This makes it easier to see where the barriers are, which is very important for contact alignment. Good contact alignment is important in this project since the superconducting contact must be placed very close to the quantum dots in order for the superconductivity to be induced into the nanowire segment via the proximity effect. Figure 3.1b shows an InAs/GaSb core-shell nanowire.

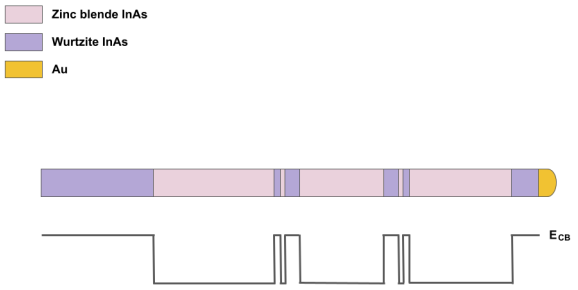


(a) InAs nanowire with WZ barriers and ZB quantum dots. $E_{CB}$ is the conduction band edge.

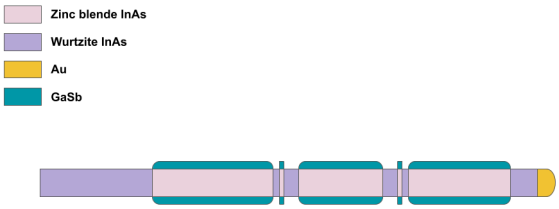


(b) InAs nanowire with WZ barriers, ZB quantum dots and a shell of GaSb.

Figure 3.1

## 3.2 Device fabrication

This section will give a detailed description of two different processing schemes used to fabricate Cooper pair splitter devices. Because several of the process steps are the same for process 1 and process 2, process 1 will be described in most detail.

### 3.2.1 Process 1

The first step in the fabrication process was to mechanically transfer the InAs/GaSb core-shell nanowires from a growth substrate to a measurement substrate. The measurement substrate was a degenerately n-doped silicon (Si) substrate with a 200 nm layer of thermally grown silicon dioxide ($SiO_2$). The substrate also had markers for electron beam lithography (EBL)-alignment, a coordinate system and 12 predefined Au pads. The back side of the Si substrate functioned as a global back gate. The substrate will also be referred to as a 'sample' and there will be several devices on each sample. To increase the control of the nanowire deposition process, a micromanipulator tool from Leica Microsystems was used.

After the nanowire deposition, a scanning electron microscope (SEM) FEI Nova NanoLab 600 was used to take images of the nanowires and their location in relation to each other and the EBL-markers. The SEM images were then imported into a LabVIEW program called "Automatic electrodes" [36]. The program was used to create electrode patterns for EBL. Additional changes to the design pattern were made in the program "Raith150". A detailed description of the contact design and the relevant design parameters can be seen in Appendix A. Figure 3.2 shows an illustration of the nanowire with two normal contacts (drains) denoted N1 and N2, four normal side gates all denoted sg and one superconducting contact (source) denoted S. Process 1 required two EBL steps. In the first step all six normal contacts were defined, while the superconducting contact was defined in the second step.

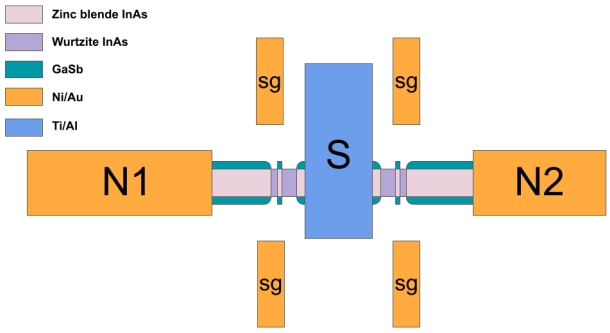


Figure 3.2: Illustration of a device fabricated according to process 1. Note that the back gate can't be seen in the figure.

The sample was then spin-coated for 40 s at 5000 rpm with polymethyl methacrylate (PMMA 950 A5), which is a positive EBL-resist, and then baked on a hot plate at 180 °C for 5 min. Then followed EBL exposure with the system Raith 150, using the created design patterns to define the contacts. Since PMMA is a positive resist the areas exposed to the electron beam were soluble in the developer solution after exposure. The developer was a mixture of methyl-isobutyl-ketone (MIBK) and isopropanol (IPA). After exposure the sample was developed in MIBK:IPA (1:3) for 40 s and then rinsed in IPA for 30 s and blow-dried with a nitrogen gas ($N_2$) gun. To remove residues of PMMA on the exposed nanowire segments oxygen plasma ashing with system New PlasmaPreen was used for 30 s. During the plasma ashing the sample was covered with a Faraday cage.

The etching of GaSb was performed in the developer MF319 with active component tetramethylammonium hydroxide (TMAH) for 3 minutes, rinsed in $H_2O$ for 1 min and blow-dried with $N_2$ gun. The next step in the fabrication process was a chemical wet etch to remove native oxides on the exposed nanowire areas. The etchant used was a mixture of hydrochloric acid (HCl) and $H_2O$ HCl(37 % bulk solution):$H_2O$ (1:20). The sample was first put in the diluted HCl for 15 s and then rinsed in $H_2O$ for 20 s. The sample was then blow-dried with a $N_2$ gun. Directly after the wet etch in HCl the sample was moved into the electron beam evaporator system Temescal E-Beam and was covered with a 25 nm layer of Ni, for better adhesion, followed by a 75 nm layer of Au.

The excess metal was then lifted off by dissolving the underlying resist using acetone heated to 65 °C. When the lift-off process was complete the sample was washed in IPA and then dried with a $N_2$ gun. The main steps for the fabrication of the normal contacts for process 1 can be seen in Figure 3.3. Note that the four side gates are not drawn and the two normal contacts are not placed exactly according to Figure 3.2. The purpose of the figure is to show simplified schematics of the different process steps.

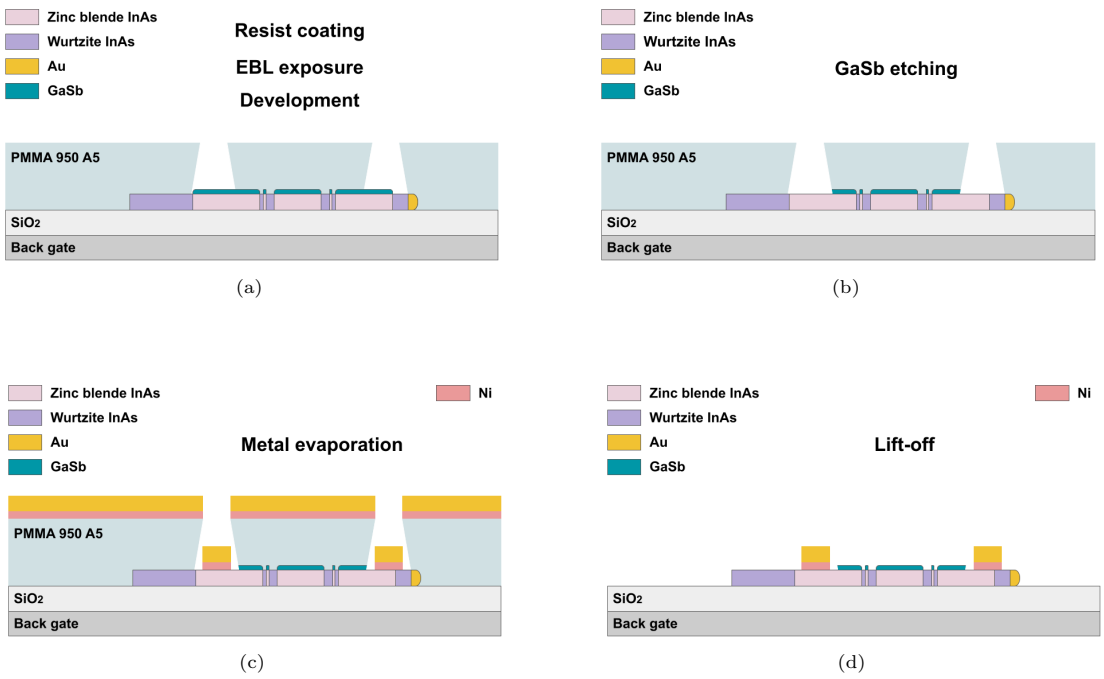


Figure 3.3: Main process steps for fabrication of the normal contacts for process 1.

Then all of the above steps from spin-coating of resist to lift-off were repeated with the difference that this time it was the superconducting contact that was defined with EBL and a layer of 5 nm thick Ti and 115 nm thick Al was evaporated. These steps are illustrated in Figure 3.4.

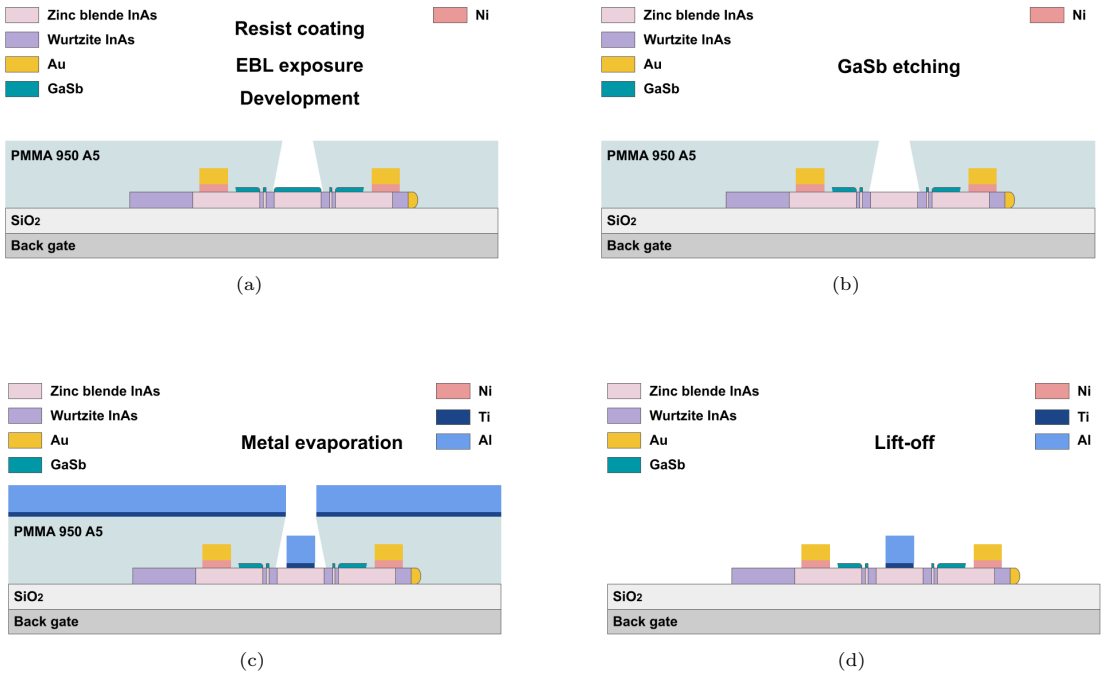


Figure 3.4: Main process steps for fabrication of the superconducting contact for process 1.

When all contacts were fabricated the sample was glued with silver glue onto a 14 pin dual in-line package with Au-pads. Aluminum wires connecting the Au pads on the sample and the Au pads on the package were formed with the wire-bonding system FS Bondtec 53XX BDA. The nanowire devices could then be connected to the macroscopic electronics used for electrical characterization.

### 3.2.2 Process 2

Process 2 can simply be explained as a method where the entire shell of GaSb is removed before any of the contacts are defined. However, it is not possible to directly place the sample with deposited nanowires in MF319, as the nanowires move during etching and thus risk being rinsed off from the sample. The idea of process 2 is to clamp the nanowire stem with resist and open up a window in the resist, which is large enough to cover the entire shell of GaSb.

The first steps in process 2 are therefore spin-coating of resist followed by EBL exposure and development. Before the GaSb etching the sample was plasma ashed for 30 s. The sample was then dipped into MF319 for 3 minutes, rinsed in $H_2O$ for 1 minute and blow-dried with a $N_2$ gun. Finally, the resist was removed in a lift-off process with hot acetone. The main steps for removal of GaSb in process 2 are illustrated in Figures 3.5a-3.5c. The subsequent steps to define the normal and the superconducting contacts were the same as in process 1, except that no etching of GaSb was performed between the plasma ash and the wet-etch in HCl. The big difference between the different methods is that process 2 requires three EBL steps, while process 1 only requires two EBL steps. The final device fabricated according to process 2 can be seen in Figure 3.5d.

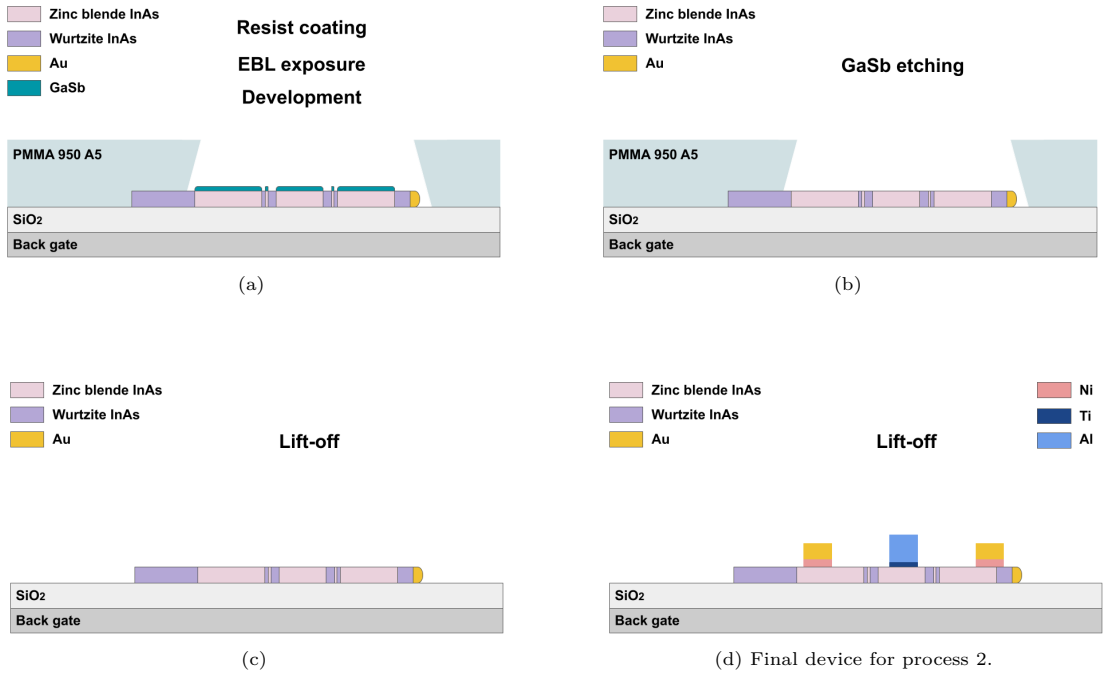


Figure 3.5: Main process steps for process 2.

Another difference between the methods was the contact design. In process 1, a design was made with four side gates. In process 2, it was chosen to only make one side gate and to make it of Ti/Al instead of Ni/Au. The reason why only one side gate was made was to facilitate the design since the contacts must be put very close to each other. Having fewer contacts also makes it possible for more devices to be cooled down simultaneously in the dilution refrigerator. The disadvantage of using only one side gate is that it becomes more difficult to control the energy levels in the quantum dots, and that it will not be possible to form any

quantum rings, which is needed for the future goal of spin-resolved CPS. The energy levels in QD1 will now only be controlled with the back gate. An illustration of a device fabricated according to process 2 with two normal contacts (drains), one superconducting side gate and one superconducting contact (source) can be seen in Figure 3.6.

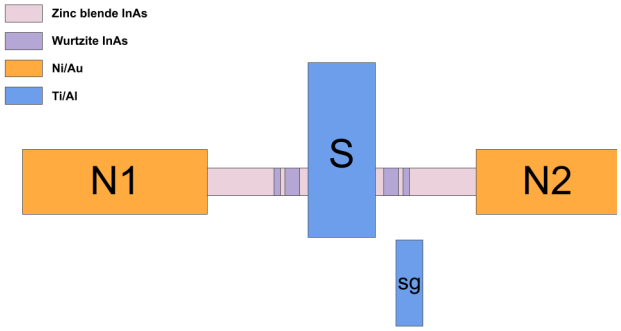


Figure 3.6: Illustration of a device fabricated according to process 2. Note that the back gate can't be seen in the figure.

## 3.3 Electrical measurements at room temperature

To determine which of process 1 and process 2 gave the best quality of the InAs-Ti/Al contact interface, electrical measurements on the devices were performed at room temperature. Two different measurements were performed using the setups illustrated in Figures 3.7a and 3.7b. Note that only the contacts involved have been drawn. In Figure 3.7a a DC voltage was applied between the superconducting contact and the normal contacts. The current through one of the normal contacts was measured with a multimeter. In Figure 3.7b a DC voltage was applied to N2 and the current through N1 was measured.

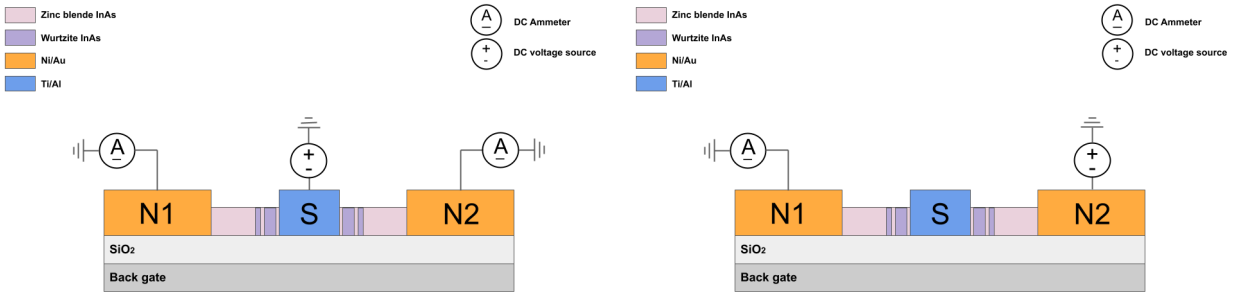


(a) Measurement setup when voltage applied between S and N. (b) Measurement setup when voltage applied between N2 and N1.

Figure 3.7

Six devices were fabricated according to process 1. These will be denoted 1a-1f. Six devices were fabricated according to process 2 and will be denoted 2a-2f. The results from the two room temperature measurements are shown in Table 3.1. The table only gives the result yes if a current was measured and the answer no if no current was measured. The two currents that were measured were current S-N using the measurement setup in Figure 3.7a and current N-N using the measurement setup in Figure 3.7b.

Table 3.1: Summary of room temperature measurements. Current S-N means S-N1 or S-N2. The current was only measured through one of the normal contacts.

| **Device** | **Current S-N (yes/no)** | **Current N-N (yes/no)** |
|---|---|---|
| 1a | yes | yes |
| 1b | yes | yes |
| 1c | no | yes |
| 1d | no | yes |
| 1e | no | yes |
| 1f | no | yes |
| 2a | no | yes |
| 2b | no | yes |
| 2c | yes | yes |
| 2d | yes | yes |
| 2e | yes | yes |
| 2f | yes | yes |

From the table it can be seen that only two of the devices fabricated according to process 1, 1a and 1b, had a current flowing from the superconducting contact. There were only two devices fabricated according to process 2, 2a and 2b, that did not have any current. All devices had a current flowing between the normal contacts, indicating that the reason why there was no current S-N was due to the superconducting contact. Subsequently, SEM images were taken on the devices to see if the superconducting contacts had been damaged or had been placed incorrectly in relation to the nanowire. Nothing like this could be seen. Therefore, it was assumed that the reason no current was flowing in the superconducting contact probably was due to a bad interface to the nanowire.

The fraction of functioning superconducting contacts increased from 1/3 to 2/3 between process 1 and process 2. One possible explanation to why process 2 seems to give better superconductor-nanowire interfaces is that process 1 may not etch away all GaSb under the contacts. This may be because there are already contacts drawn to the bond pads during the second etching step. The contacts form a circuit, in which a voltage difference between different components can occur. This voltage difference can change the etch rate or change the selectivity of the etching. However, it is important to point out that only six devices were compared for each process, which of course is a small amount. In order to be able to say with certainty that process 2 gives better superconductor-nanowire interfaces than process 1, more devices should have been tested. Another question that arises is why it is only the interface between the superconducting contact and the nanowire that seems to be bad. Why are the normal contacts not affected? This can probably be explained by the fact that the superconducting contacts have smaller areas, which means that they are more sensitive to residues of GaSb due to insufficient etching.

## 3.4 Etching of GaSb

The purpose of the experiments presented in this section was to compare three different etching cases and find out if $H_2O$ can be used as an etchant for GaSb. All experiments were performed using the process steps in Figure 3.5 for the following etching cases:

1. MF319 3 min
2. MF319 30 min
3. $H_2O$ 30 min.

SEM images of one nanowire taken before and after the etching of GaSb for the three cases can be seen in Figure 3.8. In Figures 3.8b, 3.8c 3.8e, and 3.8f the window edge of PMMA has also been drawn as a green line. For MF319 30 min, the part above the green line is covered in PMMA. For $H_2O$ 30 min, the left side of the green line is covered in PMMA.

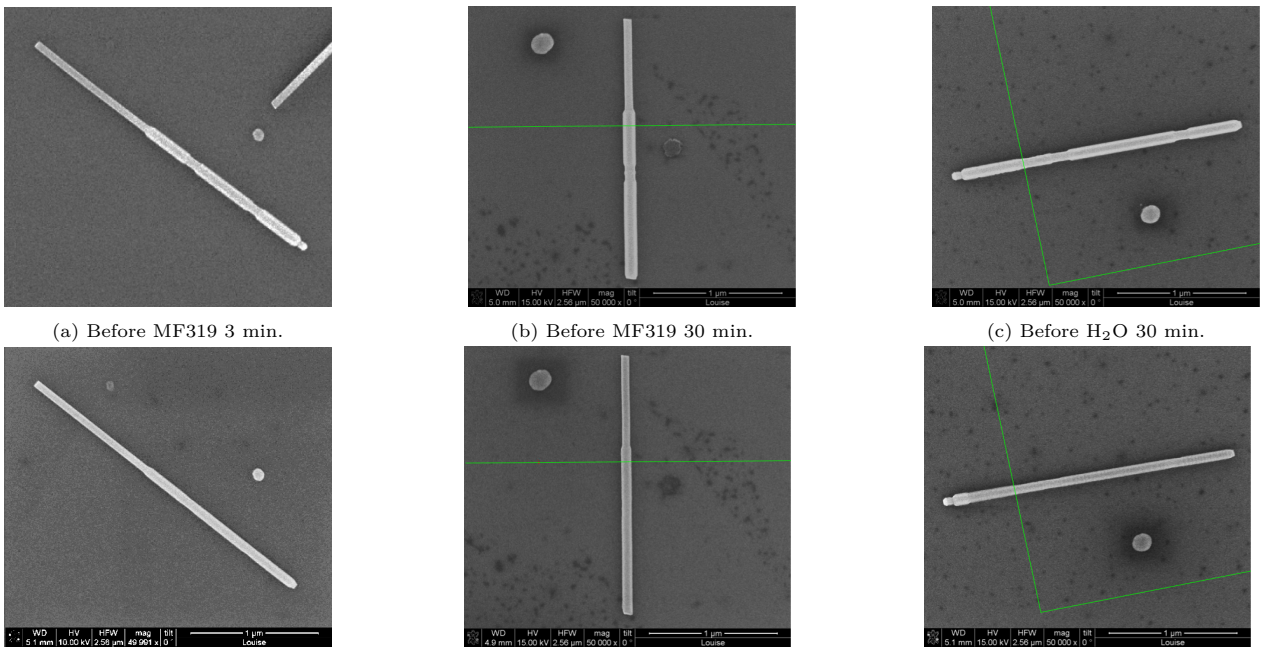

(a) Before MF319 3 min. (b) Before MF319 30 min. (c) Before $H_2O$ 30 min.

(d) After MF319 3 min. (e) After MF319 30 min. (f) After $H_2O$ 30 min.

Figure 3.8: Before etching and after etching SEM images for the three different cases. The green line is the window edge of PMMA.

From the SEM images it can be seen that the amount of GaSb has decreased in all three cases, since it is more difficult to see where the segments of WZ are. Therefore, it seeams that $H_2O$ can be used as an etchant for GaSb, which is a cleaner, cheaper and simpler process than using MF319. There was no indication that the InAs was attacked by either MF319 or $H_2O$. This is important because the goal was to etch away the shell of GaSb without affecting the InAs. In both Figure 3.8e and Figure 3.8f, it can also be seen that the amount of GaSb has decreased even outside the windows. This indicates that both MF319 and $H_2O$ creep under the resist and etch outside the intended areas. This means that the etching cannot be done very precisely.

To compare the amount of GaSb that has been etched away in the various cases the diameter of the nanowires was measured, before and after the etching of GaSb. The diameter was measured along three different points on the nanowire, A, B, and C, according to Figure 3.9a. The diameters of the nanowires were estimated using a LabVIEW program. The LabVIEW program plotted the normalized gray scale intensity along a linecut of a SEM image, where 1 equals white color and 0 equals the darkest shade of gray. The linecut had a thickness of 55 nm and is represented by the red line across point A in Figure 3.9a. The normalized gray scale intensity as a function of the distance along the linecut for a typical nanowire can be seen in Figure 3.9b. The diameter of the nanowire was chosen to be the FWHM of the intensity, i.e., the full width when the intensity equals 0.5. It is an assumption that the FWHM represents the diameter. It is possible that there is a better measure of the diameter, for example precisely when the intensity increases. As can be seen in Figure 3.9b the intensity is higher at the edges of the nanowire. This is due to the phenomenon of edge effect in SEM, which makes the edges of a specimen appear brighter, because the edges provide a larger surface area from which more secondary electrons can escape.

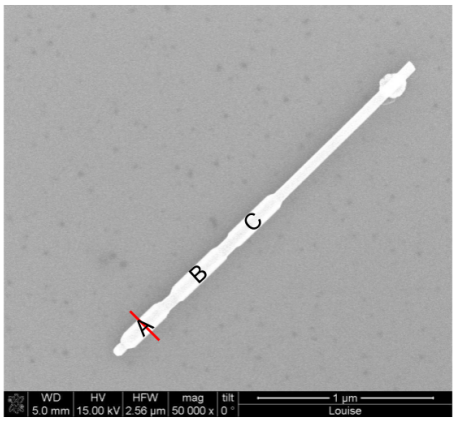


(a) Typical nanowire indicating the points A, B, and C. A red line has been drawn perpendicular along A.

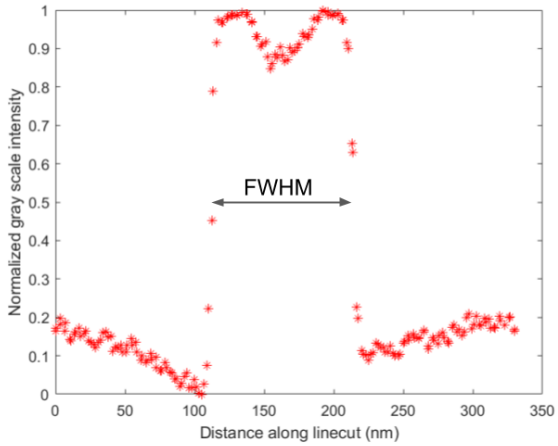


(b) Normalized gray scale intensity along the red linecut of the SEM image in Figure 3.9a. The FWHM is considered the diameter of the nanowire.

Figure 3.9

The result from the measurements for point A can be seen in Figure 3.10. The values on the x-axis indicate which nanowire is being measured. It can be seen in the figures that a total number of 16 nanowires were measured. Both figures are divided into three sections corresponding to $H_2O$ 30 min, MF319 30 min and MF319 3 min. Figures 3.10a show the diameter of the nanowires along point A before and after etching, with an estimated sample standard deviation of $s_d = 4.7$ nm. Figure 3.10b shows the diameter difference, calculated as the diameter before - the diameter after, on the nanowire along point A, with an estimated sample standard deviation of $s_\Delta = 6.6$ nm. A positive diameter difference, therefore, corresponds to a reduced diameter. In Figure 3.10b, three horizontal lines have also been drawn. The middle line corresponds to the mean value of the measuring points, while the two dashed lines correspond to the mean value $\pm s_\Delta$. The results from point B and C were very similar to point A and can be seen in Appendix B.

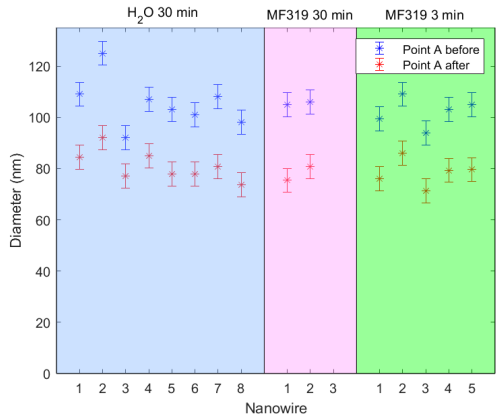


(a) Diameter before (blue) and after (red) etching for point A.

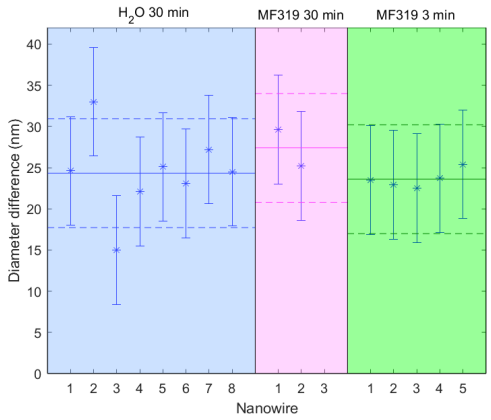


(b) Diameter difference for point A. The horizontal lines show the average diameter difference including error.

Figure 3.10

All measurements resulted in a positive diameter difference and, therefore, a reduction in the nanowire diameter, indicating that both $H_2O$ and MF319 can be used as an etchant for GaSb. Note, that the number of nanowires was few and to get a more reliable result, more nanowires should be used. There was a large overlap between the measuring points for the different cases, due to measurement uncertainties. Therefore, it was not possible to determine whether the diameter difference differed in the three cases and thus it was not possible to say which etching method is most efficient. One measurement uncertainty that was taken into account was that the diameter of the nanowires was dependent on contrast and brightening settings used in the various SEM images. Figure 3.11 shows the same SEM image taken on a nanowire. The contrast and brightness of the images have been changed after the SEM image was taken. The FWHM along the same horizontal line was measured and different FWHMs were obtained for all four contrast settings. In addition, different FWHMs were obtained for different magnifications on the SEM images, which can be seen in Figure 3.12. When measuring the diameters of the nanowires, it was also important that the chosen line was perpendicular to the nanowire growth direction, which also contributed to the measurement uncertainty. The calculations for the estimated sample standard deviations can be seen in Appendix C.

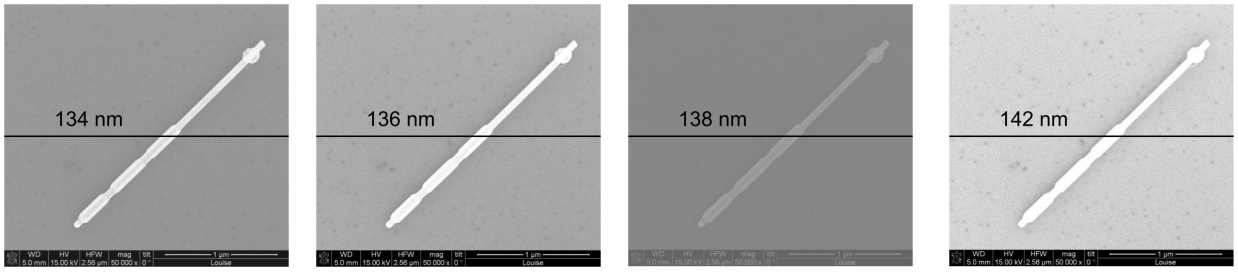


(a) (b) (c) (d)

Figure 3.11: Four different values of FWHM obtained from the same horizontal line with different contrasts and brightening settings.

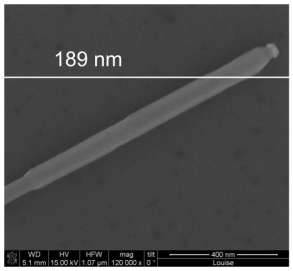


(a) Scale bar 400 nm.

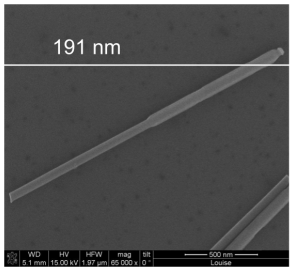


(b) Scale bar 500 nm.

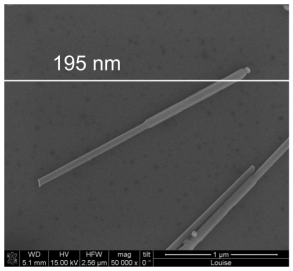


(c) Scale bar 1000 nm.

Figure 3.12: Three different values of FWHM obtained from the same horizontal line with different magnifications.

Although it was not possible to determine from the measurements of the diameters which of MF319 and $H_2O$ etches GaSb most effectively, it was suspected that $H_2O$ etches GaSb more slowly. The indication of this can be seen in Figure 3.13. From the figure it can be seen that the gold particle is still attached to the nanowire in the case of 30 min $H_2O$, while the gold particle is not attached to the nanowire in the case of 30 min MF319. This was true even for 3 min MF319. There is a short axial segment of GaSb just before the gold particle. One explanation to why the gold particle on the nanowires in the case of MF319 is no longer attached to the nanowire, is that the axial segment has been etched away and, therefore, the gold particle has fallen off. In the case of $H_2O$, the axial segment of GaSb has not been completely etched away, which has resulted in the gold particle not falling off.

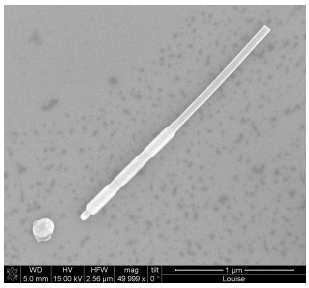

(a) Before MF319 30 min.

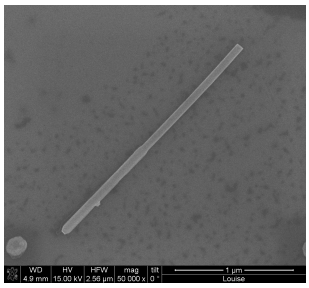

(b) After MF319 30 min.

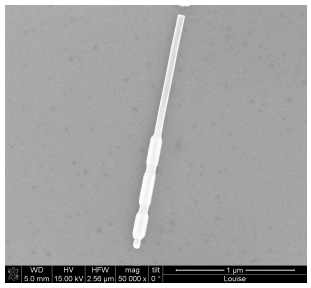

(c) Before $H_2O$ 30 min.

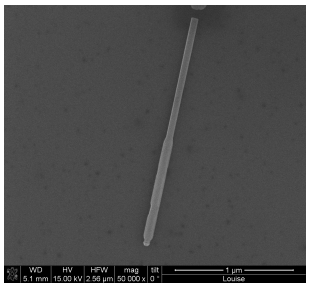

(d) After $H_2O$ 30 min.

Figure 3.13: Axial GaSb segment near Au particle etched away in MF319 but not in $H_2O$.

## 3.5 Summary processing

When comparing process 1 and process 2 for fabrication of CPS devices it was found that the fraction of devices with functioning superconducting contacts was larger for process 2 than for process 1. This might indicate that the quality of the InAs-Ti/Al contact interface gets better if the whole GaSb shell was removed before any other process step.

Three different etching cases were compared by measuring the diameter of nanowires before and after etching. It was found that both $H_2O$ and MF319 can be used to etch GaSb. Due to large measurement uncertainties it was not possible from these measurements to determine which of $H_2O$ and MF319 etched GaSb most efficiently, but when looking at the axial segment of GaSb just below the Au particle, it seems that MF319 etches faster than $H_2O$.

# Chapter 4

# Electrical measurements

This chapter presents the electrical measurements performed in a dilution refrigerator on one device fabricated according to process 2. The quantum dots were characterized, the parameters in the regime of interest were extracted and several comparisons between AC and DC measurements were made. Since different measurement techniques have been used, the details of how the measurement setups will first be presented.

## 4.1 Lock-in amplifier

Lock-in amplifiers have been widely used by the groups that investigate Copper pair splitters [10] [11] [12] [37] and will therefore also be used in this thesis. The basic principle of how a lock-in amplifier works will be discussed in this section. For details the reader is referred to Ref. [38]. Note that there are several parameters of a lock-in amplifier that will not be discussed. These parameters may be important for how well the measurements are performed but are outside the scope of this thesis.

According to Fourier's theorem almost any periodic signal can be expressed as a sum of sine terms of different amplitudes, frequencies and phases, in a Fourier series. A lock-in amplifier uses a technique to single out one of the components in the Fourier series, the one at a specific reference frequency. A lock-in amplifier can, therefore, be used to detect and measure very small AC signals that are buried in noise. The lock-in amplifier has a component called a multiplier which takes the input signal and multiplies it by an output sine wave, with a given reference frequency and a root-mean square (rms) voltage, $V_{rms}$. The rms voltage is the square root of the time average of the voltage squared and is equal to the constant DC voltage that would give the same amount of heat in a resistor. The rms voltage can be expressed as $V_{rms} = \frac{V_{pk}}{\sqrt{2}}$, where $V_{pk}$ is the peak voltage. Sine waves with different frequencies are orthogonal, which means that their inner product is zero,

$$\int_0^{2\pi} \sin(nx) \cdot \sin(mx) dx = 0 \text{ for } n, m \in \mathbb{Z} \text{ and } n \neq m. \tag{4.1}$$

Thus, the average of the product of two sine waves will become zero for all frequencies, except if the component of the input signal has exactly the same frequency as the reference signal. After the multiplier there is a low pass filter which provides the averaging and removes the products of the reference signal with all the other components. The low pass filter is set by a time constant, which is equal to 1/2f, where f is the -3 dB frequency of the filter. When the time constant is increased, the output becomes more steady and smooth, but at the cost of longer measurement times, since it takes about 5 time constants for the filter to settle to its final value.

## 4.2 Measurement setup

To be able to resolve the electronic properties of the device, the electron temperature must be well below the relevant energy scales, for example the charging energy $E_C$, the level spacing $\delta E$, the coupling $\Gamma$ and the size of the superconducting gap $\Delta$. All electrical measurements were, therefore, performed in a dilution refrigerator Triton 200 from Oxford Instruments, with a base temperature of $\approx 50$ mK. The transition temperatures, $T_c$, for aluminum and titanium are 1.2 K and 0.40 K respectively, so both elements of the Ti/Al contacts were superconducting in the refrigerator. The resistance for two lines in series in the refrigerator was approximately 6 kΩ.

To make comparisons between AC and DC measurements, three different types of measurement setups were used, which will be referred to as DC measurement, AC measurement and AC+DC measurement. The following paragraphs will cover the relevant concepts and schematics to these three measurement setups. All measurement setups were controlled with a computer via a LabVIEW program and a General Purpose Interface Bus (GPIB).

**DC measurement**
One simplified and one detailed schematic showing the nanowire with its contacts and the important circuit components can be seen in Figure 4.1. In the DC measurement a Yokogawa GS200 DC voltage source was used to apply a DC voltage over the superconducting contact relative to ground. The superconducting contact is denoted S in Figure 4.1. The DC voltage source was in series with a 1:1000 voltage divider. DC voltages were also applied over the side gate, denoted sg, and the back gate. The side gate and the back gate were altered in the same way in all three measurement setups and will not be mentioned in the remaining cases. The side gate mainly controlled the energy levels in the right quantum dot, while the back gate controlled the energy levels in both quantum dots. To measure the currents through the quantum dots, the normal contacts, denoted N1 and N2, were each connected to a Femto DLPCA-200 voltage-to-current amplifier which in turn was connected to a HP 34401A multimeter.

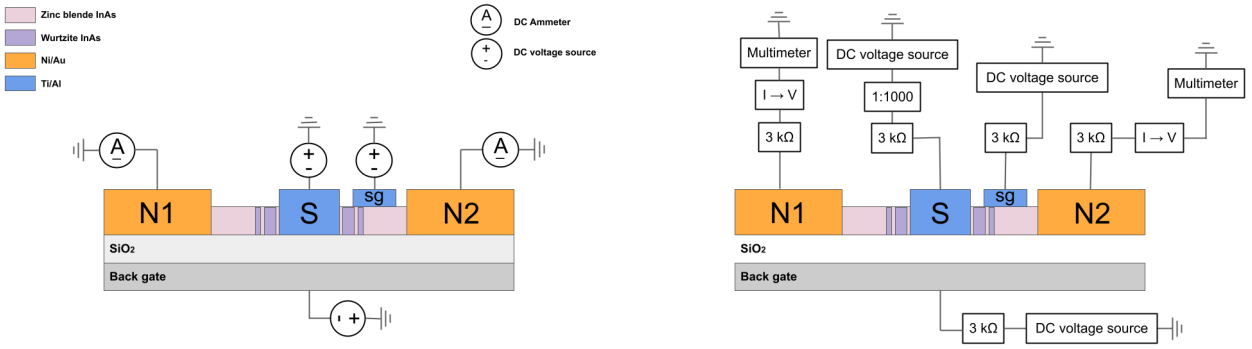


(a) Simplified.

(b) Detailed.

Figure 4.1: DC measurement setup.

### AC measurement

In the AC measurement, an AC voltage was applied from the output of a lock-in amplifier Stanford SR 830 via a 1:10000 voltage divider. Each of the two quantum dots were connected to a capacitor of 6.7 µF. The purpose of the capacitors was to eliminate any possible DC offset between the AC voltage output and the AC current input, which measures the AC current from the two quantum dots. Figure 4.2 shows the most important circuit components of the AC measurement.

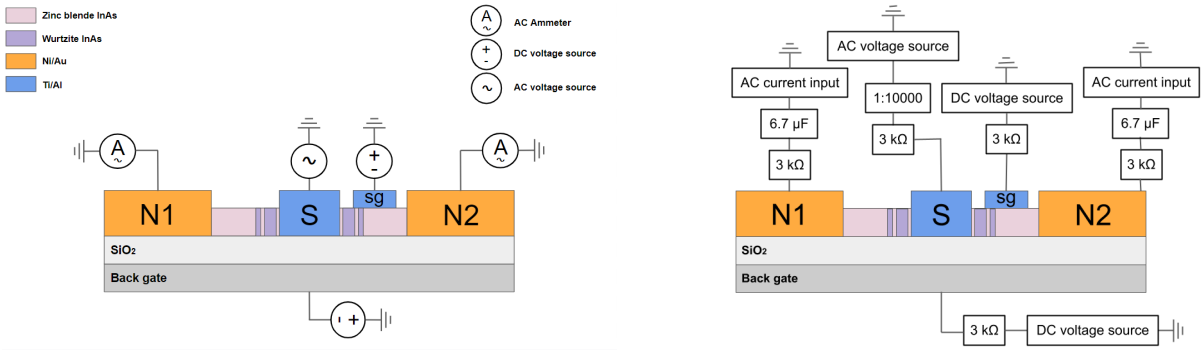


(a) Simplified.

(b) Detailed.

Figure 4.2: AC measurement setup.

### AC+DC measurement

The AC+DC measurement applied an AC voltage from the AC voltage output of the lock-in amplifier, superimposed with a DC voltage from the DC voltage source, to the superconducting contact. The dividers were 1:100000 for the AC voltage and 1:1000 for the DC voltage. The divider was a box with three resistors according to Figure 4.3. A divider box corresponding to the lower part of Figure 4.3 was used in the 1:1000 divider for the DC measurement setup.

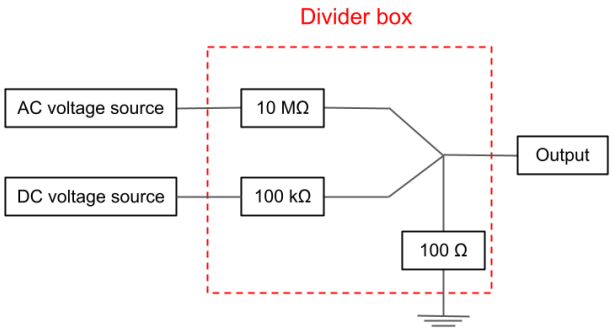


Figure 4.3: Illustration of the voltage divider box for the AC+DC measurement setup.

The two normal contacts were once again connected to the AC current input of two lock-in amplifiers, but this time without any capacitors that otherwise would interfere with the DC grounding of N1 and N2, which would result in no voltage drop over the quantum dots. A schematic of the important components for the AC+DC measurement can be seen in Figure 4.4.

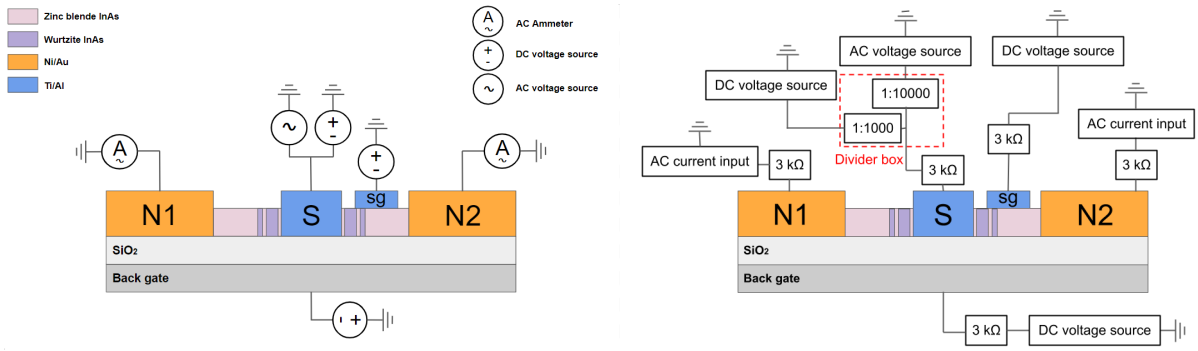


(a) Simplified.

(b) Detailed.

Figure 4.4: AC+DC measurement setup.

## 4.3 Results

This section covers the electrical measurements made on one device, fabricated according to process 2. The first and final SEM image of the device can be seen in Figure 4.5. By overlaying the first SEM image with the final SEM image, it was possible to estimate where the segments of WZ were located. The WZ barriers are colored in green in Figure 4.5b. The approximate position of the two quantum dots and their barriers are indicated in Figure 4.5b by their respective names, QD1 and QD2. Note that 4.5a is zoomed in from a low resolution SEM image and the contrasts in the two figures are very different. The distance between the quantum dots was approximately 550 nm. A superconducting contact of Ti/Al with a thickness of 5 nm/115 nm and a width of 400 nm was placed between the dots. The side gate of Ti/Al mainly controlled the energy levels in QD2 and two normal contacts of Ni/Au were placed at both ends of the InAs nanowire.

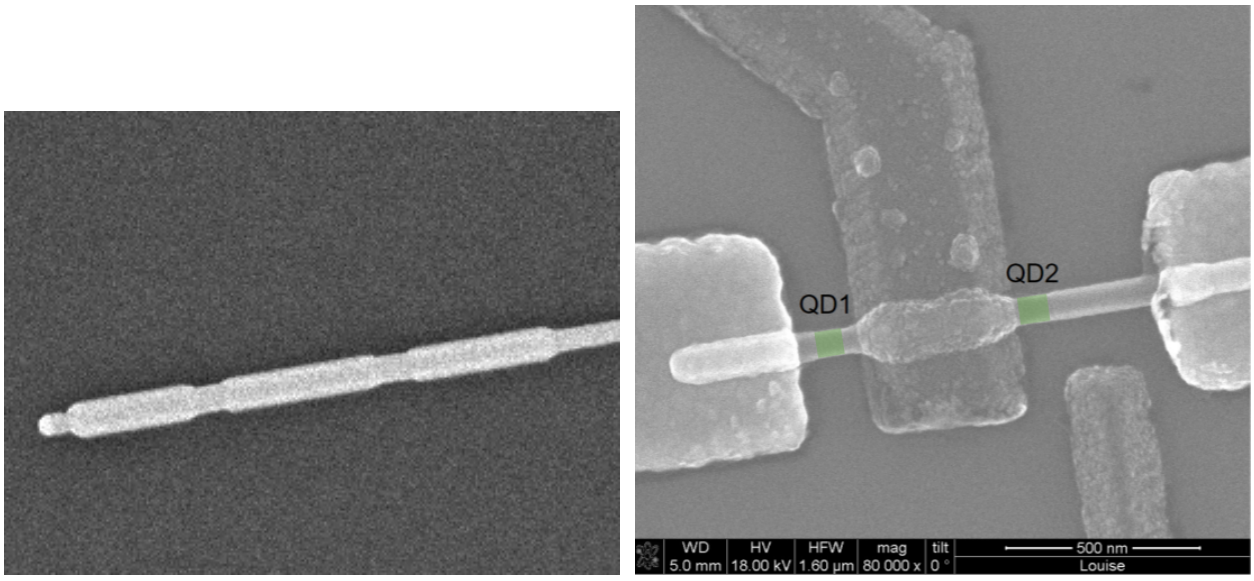


(a) First image. Note the indentations in the GaSb shell indicating the location of the WZ barriers.

(b) Final image. The WZ segments have been colored in green and the quantum dots are denoted QD1 and QD2.

Figure 4.5: SEM images of the device.

### 4.3.1 Charge stability diagram

Charge stability diagrams were recorded to characterize the two quantum dots in the nanowire. The measurements were performed in the dilution refrigerator with the DC measurement technique explained in Section 4.2, where $V_{sd}$ is the voltage applied to the superconducting contact and $V_{bg}$ is the voltage applied to the back gate. The subscripts 1 and 2 will hereinafter refer to QD1 and QD2. The current flowing to respective normal contact, $I_1$ and $I_2$, was measured. In Figure 4.6a the differential conductance, $\frac{dI_1}{dV_{sd}}$, is plotted as a function of $V_{sd}$ and $V_{bg}$, while a similar measurement for QD2 can be seen in Figure 4.6b.

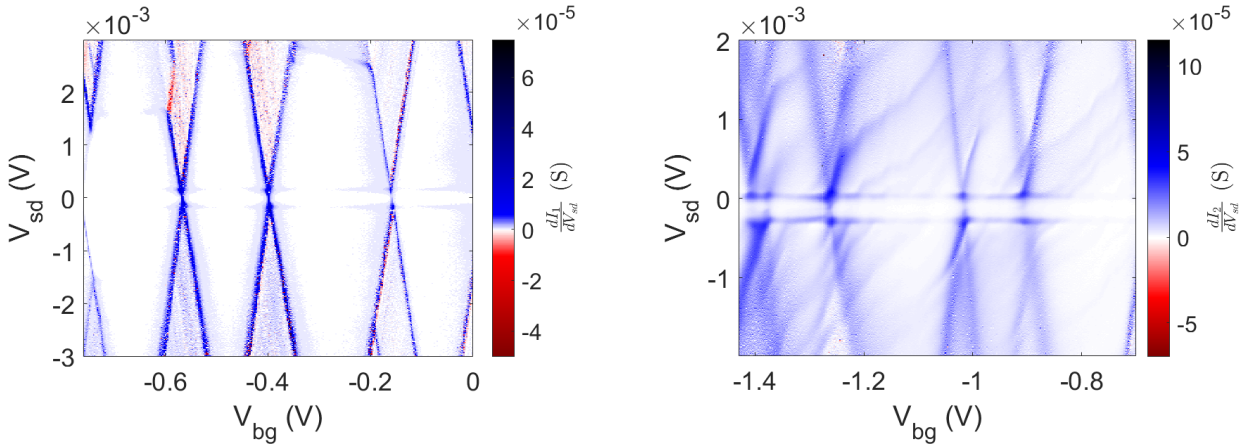


(a) QD1.

(b) QD2.

Figure 4.6: Charge stability diagrams. The differential conductances, $\frac{dI_1}{dV_{sd}}$ and $\frac{dI_2}{dV_{sd}}$, as functions of source-drain voltage, $V_{sd}$, and back gate voltage, $V_{bg}$.

Both figures look rather similar to the schematic charge stability diagram in Figure 2.5, with a pattern of small and large diamonds, which indicate that in this system there seems to be resolved quantized single-particle energy levels that are degenerate in spin. This leads to an odd-even behavior. The energy required to add the first electron to the quantum dot is $E_{add} = \delta E + E_C$, while populating the same single-particle energy level with a second electron of opposite spin costs only $E_{add} = E_C$. A clear shell-filling pattern is desirable to detect Cooper pair splitting, since this would reduce the risk of unwanted correlations between the electrons in the quantum dot as discussed in Section 2.3.

The additional energy, $E_{add}$, for the small and large diamonds in QD1 was estimated to $E_{C1} = 5.6$ meV and $E_{C1} + \delta\varepsilon_1 = 7.0$ meV, respectively, from the height of the diamonds, according to Equations (2.9) and (2.10). From Equation (2.6) the level spacing could then be estimated to $\delta E_1 = 1.4$ meV. By measuring the width of the small diamond to 0.18 V, a value of the back gate lever arm could be estimated to $\alpha_{g1} = \frac{0.0056}{0.18} \approx 0.031$ using Equation (2.11). Similarly, $E_{C2}$ was estimated to 2.7 meV, $\delta E_2$ to 2.6 meV and $\alpha_{g2}$ to 0.021. Note that it was more difficult to estimate the values for QD2, since the edges of the diamonds were less sharp than for QD1.

It appears that QD2 does not have the same ideal behavior as QD1. Inside the diamonds in QD1, the conductance is almost zero, which indicates that the diamonds are in Coulomb blockade, while there are several blue conductance stripes in the diamonds for QD2. These stripes may be due to a second unintended quantum dot that may have arisen due to defects in the nanowire.

In both 4.6a and 4.6b it is possible to distinguish the superconducting gap around $V_{sd} = 0$ V similar to the illustration in Figure 2.6. However, it seems that the gap for QD2 is not centered around $V_{sd} = 0$ V, which indicates that there is a DC offset between the voltage source and the voltage-to-current amplifier. To determine the size of the superconducting gaps and the DC offsets, the differential conductances were plotted together as functions of the source-drain voltage for a fixed back gate voltage of $V_{bg} = -0.43$ V, where the gaps could be seen relatively clearly in both quantum dots. See Figure 4.7, where the differential conductance of QD1 has been multiplied by a factor of 100 to more easily study the overlap between the gaps.

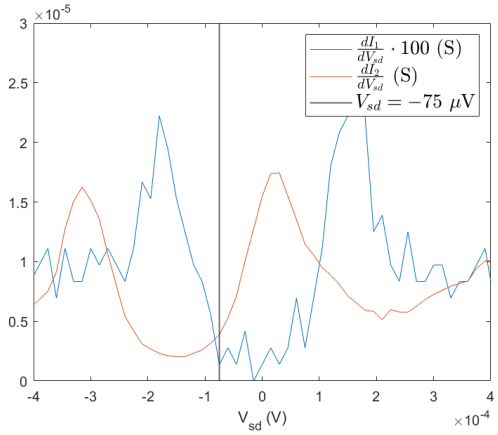


Figure 4.7: Differential conductances, $\frac{dI_1}{dV_{sd}}$ and $\frac{dI_2}{dV_{sd}}$, as functions of the source-drain bias, $V_{sd}$, showing the superconducting gaps for QD1 and QD2. The differential conductance for QD1 has been multiplied with a factor of 100. A black vertical line has been drawn at $V_{sd} = -75$ µV.

The superconducting gap looks noisier in QD1 and the conductance is much lower than in QD2. The sizes of the two gaps are approximately $\Delta_1 = \Delta_2 = 170$ µeV, which is rather close to the gap size at zero temperature of 182 µeV predicted by Equation (2.13) with $T_c = 1.2$ K. The offsets from zero bias are approximately $\delta_{DC1} = -10$ µV and $\delta_{DC2} = -145$ µV. It is important to point out the fairly large DC offset between the two amplifiers, since this might affect Cooper pair splitting measurements. An illustrative sketch of the DC offsets can be seen in Figure 4.8. The figure is drawn such that $\mu_{QD1} = \mu_S = \mu_{QD2}$. The figure also shows the superconducting gap.

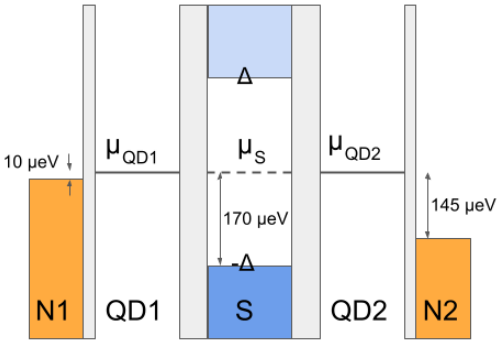


Figure 4.8: Illustration of the device in energy-space indicating the DC offsets between the voltage source and the voltage-to-current amplifiers.

In Figure 4.7 a black vertical line has also been drawn at $V_{sd} = -75$ µV. The line represents the source-drain voltage chosen to be applied over the superconducting contact in future Cooper pair splitting measurements. This source-drain voltage was chosen because it is located inside the superconducting gap for both quantum dots. As can be seen from the figure, there are not many source-drain voltages that do. If a slightly more negative source-drain voltage is applied, the edge of the gap for QD1 might be reached. And if a slightly less negative voltage than -75 µV instead is applied, the edge of the gap for QD2 might be reached. This, of course, makes it difficult to perform Cooper pair splitting measurements, as it is not easy to ensure that both quantum dots are within the superconducting gap at the same time.

Something that further complicates this problem is that the offset between the amplifiers changes slightly depending on the amplification range used. In addition, the size of the superconducting gap changes for different conductivities of the quantum dot. This is due to the fact that the resistance of the external circuit is generally comparable to the resistance of the device. The conductance changes particularly with the back gate voltage and therefore the gap size may also change with the back gate voltage. If the DC offsets and the size of the gaps change so much that the two gaps do not overlap at all, it might be difficult to detect Cooper pair splitting and this is, therefore, a drawback with the DC measurement technique.

### 4.3.2 DC measurements on conductance peaks

This section presents DC measurements made on Coulomb oscillation peaks. In all measurements, the amplifier with the least DC offset has been used. During the measurements, the quantum dot not being measured was floating. In Figure 4.9, the conductance of QD1, $G_1$, is plotted as a function of energy, $E$, for $V_{sd} = 10$ µV. The energy axis has been obtained by multiplying the back gate voltage by the back gate lever arm, $\alpha_{bg1}$, which was calculated in the previous section. In these measurements, the DC offset between the voltage source and the voltage-to-current amplifier has been taken into account, which means that a slightly higher voltage has been applied to the superconducting contact, but which should correspond to an effective source-drain bias of $V_{sd} = 10$ µV. The data in the figure has been fitted to two different curves, one corresponding to the weak-coupling regime and one corresponding to the strong-coupling regime, discussed in Section 2.1.2.

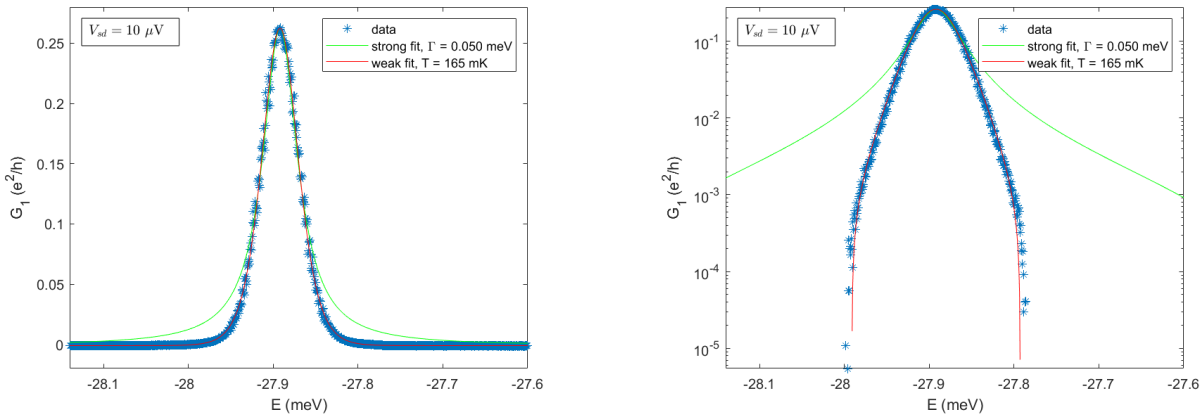


(a) Normal scale.

(b) Logarithmic scale.

Figure 4.9: DC measurement on Coulomb peak for QD1 showing the conductance, $G_1$, as a function of the energy, $E$. The data points are fitted to the strong- and the weak-coupling regime.

The data points seem to fit better according to the weak-coupling regime, since the curve corresponding to the strong-coupling regime is too wide at the bottom of the peak. To see the differences more clearly, the same data are plotted on a logarithmic scale in Figure 4.9b. The FWHM of the peak was 0.050 meV and the maximum conductance of the peak was approximately 0.26 $e^2/h$. The red curve is expressed according to Equation (2.7) with an electron temperature of 165 mK, corresponding to 14 µeV. The Coulomb peak was measured at $V_{sd} = 10$ µV, which leads to an additional broadening of the peak. The estimated electron temperature can therefore only be seen as an upper bound. A similar measurement was made for QD2 and the result can be seen in Figure 4.10a on a normal scale and in Figure 4.10b on a logarithmic scale.

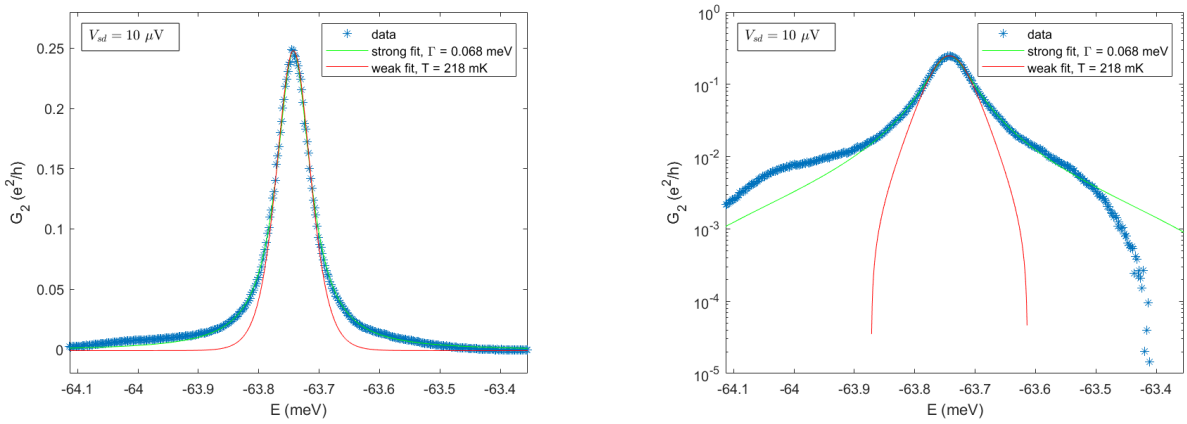


(a) Normal scale.

(b) Logarithmic scale.

Figure 4.10: DC measurement on Coulomb peak for QD2 showing the conductance, $G_2$, as a function of the energy, $E$. The data points are fitted to the strong- and the weak-coupling regime.

Unlike QD1, it seems that this Coulomb peak for QD2 is more in line with the strong-coupling regime, because the bottom part of the peak is rather wide. However, it can be seen in Figure 4.10b that the strong fit does not really follow the measuring points at the far end of the peak. The FWHM of the peak was 0.068 meV and the maximum conductance was approximately 0.25 $e^2/h$. The green curve is expressed according to Equation (2.8) with $\Gamma = 0.068$ eV. Equation (2.8) also says that,

$$\Gamma_S \Gamma_N = \frac{\Gamma^2 G_{max}}{4}, \tag{4.2}$$

where $G_{max}$ is expressed in units of $e^2/h$. By combining (4.2) with $\Gamma = \Gamma_S + \Gamma_N$ one gets two solutions,

$$\Gamma_1 = \frac{\Gamma}{2} + \sqrt{\left(\frac{\Gamma}{2}\right)^2 - \frac{\Gamma^2 G_{max}}{4}} \tag{4.3}$$

and

$$\Gamma_2 = \frac{\Gamma}{2} - \sqrt{\left(\frac{\Gamma}{2}\right)^2 - \frac{\Gamma^2 G_{max}}{4}}. \tag{4.4}$$

Here, the indices 1 and 2 have replaced $S$ and $N$ because from these equations it is not possible to determine which barrier is which. But it is possible to find the asymmetry between $\Gamma_1$ and $\Gamma_2$. Using $\Gamma = 0.068$ meV and $G_{max} = 0.25\ e^2/h$ gives $\frac{\Gamma_1}{\Gamma_2} \approx 14$, which means that QD2 is 14 times stronger coupled to one of the contacts compared to the other. According to Section 3.1 and Figure 3.1, the nanowires were designed to fulfill the requirement $\Gamma_N > \Gamma_S$. Based on this, the following assumption was made, $\Gamma_N = 14\Gamma_S \rightarrow \Gamma_N = 0.064$ meV. Note, however, according to Figure 4.5b, it is possible that the superconducting contact covers parts of the innermost barrier for QD2. If this is the case, this can lead to a narrower barrier and thus a stronger coupling, $\Gamma_S$, between QD2 and S.

The regime of interest was presented in Equation (2.23) as,

$$\begin{cases} \Delta, E_C, \delta E > \Delta\mu > \Gamma_N, k_B T \\ \Gamma_N > \Gamma_S \end{cases} . \tag{4.5}$$

The equation says that during future Cooper pair splitting measurements, a source-drain voltage should be applied to the superconducting contact to create the difference of $\Delta\mu$ in chemical potential to the normal contacts. Once again, there is a problem with the DC offset between the amplifiers. From section 4.3.1 the offsets were estimated to $\delta_{DC1} = -10$ µV and $\delta_{DC2} = -145$ µV, and the applied source-drain voltage was suggested to be $V_{sd} = -75$ µV to be inside the superconducting gap for both dots. With these values the difference in chemical potential, $\Delta\mu = \mu_S - \mu_N$ can be calculated to $\Delta\mu_1 = -65$ µeV and $\Delta\mu_2 = 70$ µeV. Figure 4.11 have been drawn to illustrate this.

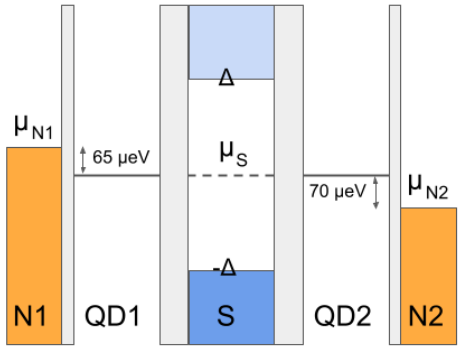


Figure 4.11: Illustration of the device in energy-space indicating the alignment of the chemical potentials when $V_{sd} = -75$ µV have been applied over the superconducting contact.

One problem can be seen from this figure, namely that $\mu_{N1} > \mu_S$, which should not be the case for ideal detection of Cooper pair splitting according to Equation (2.15). In this case, the electrons tunnel into S from N1, instead of the other way around, which makes it very unlikely to see Cooper pair splitting.

A summary of the important characteristics of the quantum dots, regarding the regime of interest, can be seen in Table 4.1. QD1 was assumed to be in the weak-coupling regime and QD2 was assumed to be in the strong-coupling regime. This is why no exact value of $\Gamma_N$ for QD1 and $k_B T$ for QD2 was calculated in the yellow boxes in the table. These have instead only been given an upper bound. In the weak-coupling regime, $\Gamma \ll k_B T$, and in the strong-coupling regime, $\Gamma \gg k_B T$. Together with the assumption that $\Gamma_N > \Gamma_S$, it was assumed that $\Gamma_N \ll 14$ µeV for QD1 and $k_B T \ll 64$ µeV for QD2.

Table 4.1: Summary of DC measurements. The yellow boxes have no specific value, only an upper bound.

| **Characteristics** | **QD1** | **QD2** |
|---|---|---|
| Charging energy, $E_C$ (meV) | 5.6 | 2.7 |
| Level spacing, $\delta E$ (meV) | 1.4 | 2.6 |
| Superconducting gap, $\Delta$ (µeV) | 170 | 170 |
| $k_BT$ (µeV) | 14 | $\ll 64$ |
| Coupling strength to normal contact, $\Gamma_N$ (µeV) | $\ll 14$ | 64 |
| Asymmetry, $\frac{\Gamma_N}{\Gamma_S}$ | - | 14 |
| Difference in chemical potential, $\Delta\mu$ (µeV) | -65 | 70 |

All inequalities are met, except that $\Delta\mu_1$ is negative, which means that the device is not within the desired regime of interest. It is important to consider that only one Coulomb peak has been measured for each quantum dot. The characteristics in Table 4.1 vary depending on the voltages applied to the gates.

To summarize, there are several disadvantages with DC measurements. In section 4.3.1 it was revealed that the DC offset between the amplifiers makes it difficult to ensure that both quantum dots are within the superconducting gap at the same time, which makes it difficult to detect CPS. In addition, in Section 4.3.2, it was shown that the DC offset between the amplifier and the voltage source can give rise to a situation where $\mu_{N1} > \mu_S$, which makes electrons tunnel to S form N1. This situation is not ideal for CPS according to the regime of interest and it seems very unlikely that CPS will be detected in this device with the DC measurement technique.

### 4.3.3 AC measurements on conductance peaks

To get around the problems with the DC offsets in the DC measurements, it is possible to turn to AC measurements. The question is, what new problems arise instead?

In Figure 4.12, the same Coulomb peak for QD1 as measured in Figure 4.9, has been measured by the AC measurement setup, as described in Section 4.2. The current input of the lock-in amplifier had a 1 kΩ impedance [38]. The same input impedance was chosen for the DC measurements to make sure that the different measurement techniques were as comparable as possible. The input impedance in the DC measurement depends on the amplifier range used for the voltage-to-current amplifier [39]. The output of the lock-in amplifier was a sine wave with a reference frequency of 63.4 Hz, a time constant of 300 ms and a rms voltage of $V_{AC} = 10$ µV. The rms voltage has in this thesis been chosen as the closest possible equivalent to a DC voltage, since it is equal to the value of the constant DC voltage that would produce the same power dissipation in a resistive load. The conductance of QD1, defined in this thesis as, $G_1 = \frac{I_1}{V_{AC}}$, is plotted both in normal scale and in a logarithmic scale as a function of the energy, E. The data in the figure has also been fitted to two different curves, one corresponding to the weak-coupling regime and one corresponding to the strong-coupling regime.

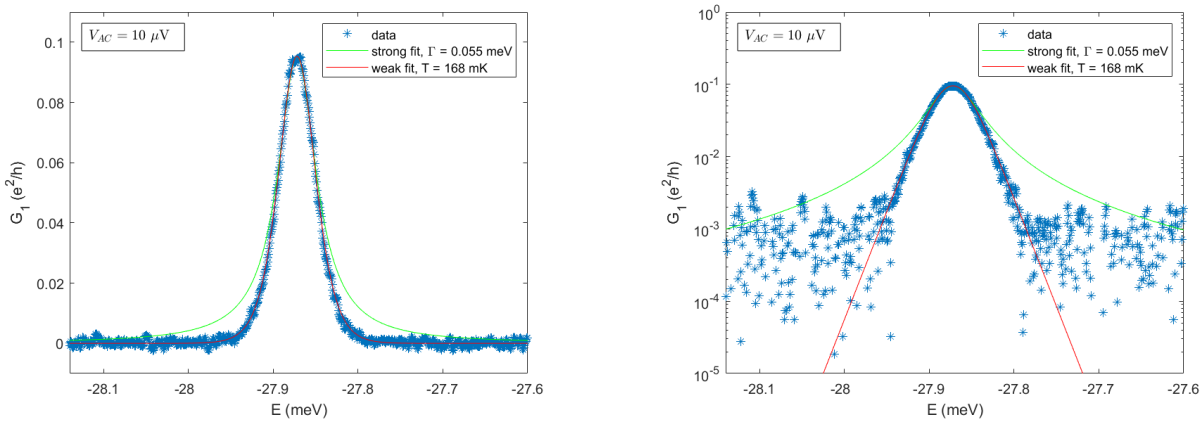


(a) Normal scale.

(b) Logarithmic scale.

Figure 4.12: AC measurement on Coulomb peak for QD1 showing the conductance, $G_1$, as a function of the energy, $E$. The data points are fitted to the strong- and the weak-coupling regime.

It can be seen that the Coulomb peak for QD1 still seems to agree best with the curve described by the weak-coupling regime. The electron temperature and the FWHM of the peak have increased slightly to 168 mK, corresponding to 15 µV, and 0.055 meV. The maximum conductance of the peak has clearly decreased to approximately 0.095 $e^2/h$. A similar AC measurement was also made for QD2, corresponding to the same peak as in the DC measurement in Figure 4.10, to see if the same differences as for QD1 appeared. The result can be seen in Figure 4.13.

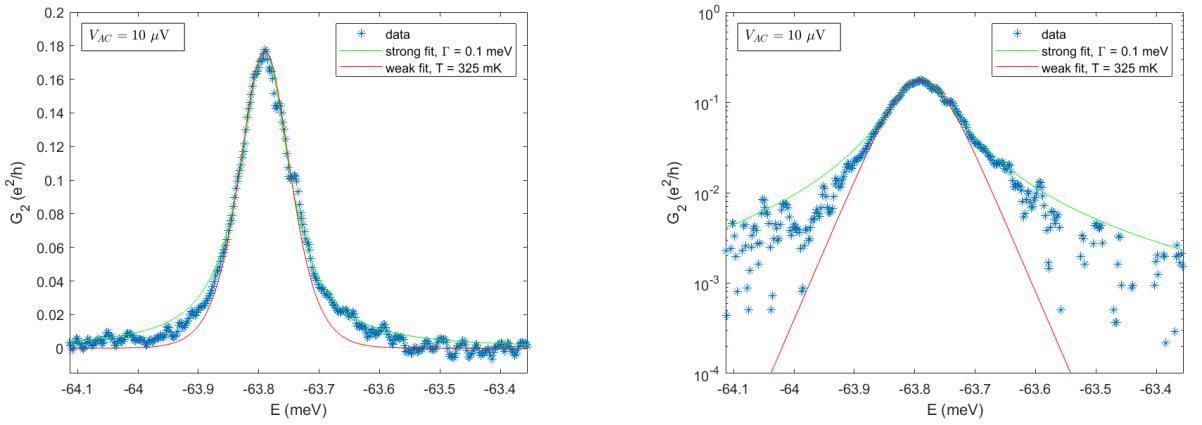


(a) Normal scale.

(b) Logarithmic scale.

Figure 4.13: AC measurement on Coulomb peak for QD2 showing the conductance, $G_2$, as a function of the energy, $E$. The data points are fitted to the strong- and the weak-coupling regime.

The data points for QD2 still seem to agree best with the strong-coupling regime, which is most clearly visible on the right side of the peak. The FWHM of the peak has increased to 0.1 meV and the maximum conductance has decreased to approximately 0.18 $e^2/h$.

In future CPS measurements with the AC technique, it was chosen that $V_{AC} = |V_{sd}| = 75$ µV, so that the AC measurement should be comparable with the DC measurement. This would result in a difference in chemical potential of $\Delta\mu = \Delta\mu_1 = \Delta\mu_2 = eV_{pk} = \sqrt{2} \cdot 75$ µeV $\approx 106$ µeV. $\Delta\mu$ is still only positive 50 % of the time since the applied voltage to the superconducting contact is alternating. This also means that $\mu_N > \mu_S$ 50 % of the time. An illustration of the device indicating the alignments of the chemical potentials can be seen in Figure 4.14.

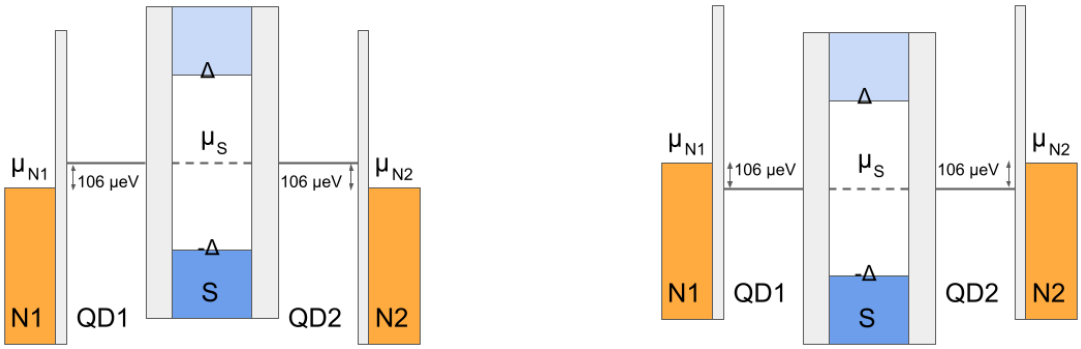


Figure 4.14: Illustration of the device in energy-space showing the alignment of the chemical potentials when an alternating voltage of $V_{AC} = 75$ µV have been applied over the superconducting contact. Note the oscillating behaviour between Figures 4.14a and 4.14b.

To consider the possibilities of detecting CPS with no DC offset, values for $k_BT, \Gamma_N$ and the asymmetry $\frac{\Gamma_N}{\Gamma_S}$ were calculated for the AC measurements and are summarized in Table 4.2. The same calculations and assumptions made for the DC measurements have also been made for the AC measurements.

Table 4.2: Summary of AC measurements. The yellow boxes have no specific value, only an upper bound.

| **Characteristics** | **QD1** | **QD2** |
|---|---|---|
| $k_BT$ (µeV) | 15 | $\ll 95$ |
| Coupling strength to normal contact, $\Gamma_N$ (µeV) | $\ll 15$ | 95 |
| Asymmetry, $\frac{\Gamma_N}{\Gamma_S}$ | - | 21 |
| Difference in chemical potential, $\Delta\mu$ (µeV) | $\pm 106$ | $\pm 106$ |

All inequalities are met, if one disregards that $\Delta\mu$ is negative 50 % of the time. This means that the device probably is within the desired regime of interest and the possibility of detecting CPS is probably higher with the AC measurement technique than with the DC measurement technique. To make the device end up in the regime of interest the whole time, it is maybe possible to make an AC+DC measurement, with a small DC bias superimposed with the AC biasing, to ensure that $\Delta\mu = \Delta\mu_S - \Delta\mu_N > 0$, but no such measurement have been made in this thesis.

The reason why the AC measurement gave Coulomb peaks with lower maximum conductance can possibly be because the DC offsets have not been properly compensated for, which may mean that a larger effective voltage has been applied between the superconducting contact and the normal contact in the DC measurements. A larger effective voltage would give a higher conductance. One problem with this scenario is that if the DC measurement had a higher effective voltage applied, the peak would probably also be wider, since this would result in a bigger bias window. But instead, the width of the DC peaks are smaller than the AC peaks, which indicates that an insufficient compensation of the DC offset is probably not the main reason for the differences between the DC and AC measurements.

The most likely reason that the AC measurements resulted in broader FWHMs and lower signals is that the settings such as rms voltage and reference frequency were not optimally chosen. Other groups with different settings may get a different result when comparing DC and AC measurements. The rms voltage multiplied with the elementary charge was 10 µeV, which is the same order of magnitude as the temperature estimated to $k_BT \approx 15$ µV. A lower rms voltage would maybe result in less broadening of the peaks in the AC measurements. A disadvantage of AC measurements is that the outcome of the measurements depends on how well chosen the various parameters were. Less optimization is required for a DC measurement, which therefore makes the DC measurement much simpler and less time-consuming. The conclusion with the comparisons between DC and AC measurements is that it is difficult to make good AC measurements, but they have the advantage of eliminating the problems with DC offsets.

### 4.3.4 Yu-Shiba-Rusinov states

Figure 4.15 shows a charge stability diagram of QD1 for back gate voltages between 0 V and 1 V. Inside the superconducting gap, several Yu-Shiba-Rusinov states, similar to the qualitative sketches illustrated in Figure 2.10, can be seen. YSR states could be seen continuously up to $V_{bg} = 10$ V, but could not be seen for lower gate voltages, where the gap could not be seen clearly either. It looks like the YSR state around 0.4 V more resembles a stronger coupling to the superconductor, as in Figure 2.10b, while it looks like the YSR state at around 0.7 V has a weaker coupling to the superconductor, as in Figure 2.10a. This, however, is difficult to determine because the charging energy varies for the different diamonds.

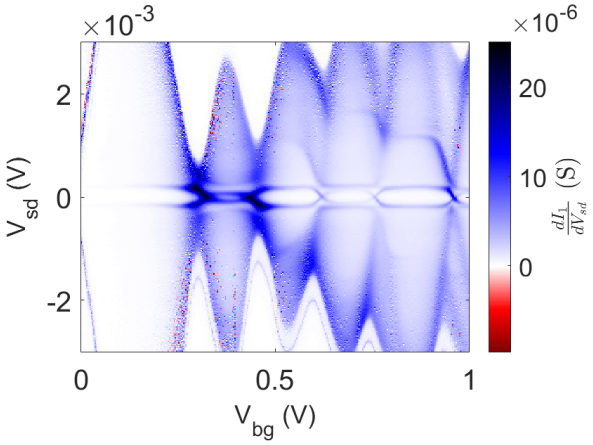


Figure 4.15: Charge stability diagram showing YSR states in QD1. The differential conductance, $\frac{dI_1}{dV_{sd}}$, as a function of the source-drain bias, $V_{sd}$, and the back gate voltage, $V_{bg}$.

Although sub-gap states have been well studied in several different superconductor-semiconductor nanostructures [40][41] and also in InAs nanowires with phase-defined quantum dots [42], they have an interesting connection to CPS. In devices with YSR states non-local signals can arise caused by the Shiba-assisted local pair tunneling (SPT) process instead of the desired CPS process, as discussed in Section 2.4. In a Cooper pair splitter with strong superconductor-dot coupling, the non-local signal has contributions from both CPS and SPT. This means that if a non-local signal is detected, it is unjustified to interpret the entire non-local signal as CPS and more efforts are required to distinguish which part of the signal is caused by CPS and which part is caused by SPT.

The small energy scales of the YSR states were used to make comparisons between DC and AC+DC measurements. The YSR state at $V_{bg} \approx 0.4$ V in Figure 4.15 was chosen to be studied in more detail. In Figure 4.16 the differential conductance, $\frac{dI_1}{dV_{sd}}$, can be seen as a function of the source-drain bias and the back gate voltage. The measurement was performed with the AC+DC measurement setup as described in Section 4.2. The reference frequency was 63.4 Hz, the rms voltage was 10 µV and the time constant was 300 ms.

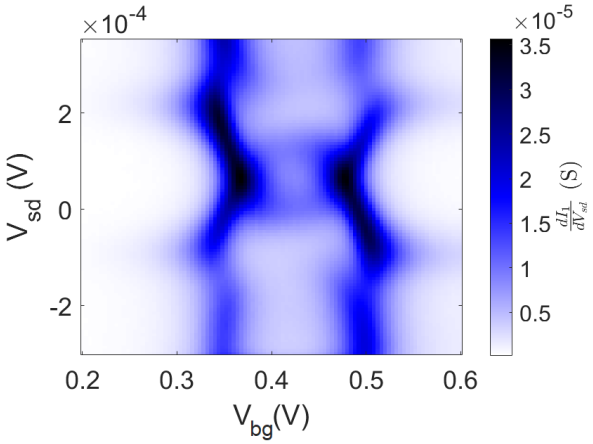


Figure 4.16: AC+DC measurement of YSR state in QD1. The differential conductance, $\frac{dI_1}{dV_{sd}}$, as a function of the source-drain bias, $V_{sd}$, and the back gate voltage, $V_{bg}$.

To study the YSR states with an applied magnetic field, a fixed back gate voltage of $V_{bg} = 0.42$ V was chosen and the magnetic field, $B_{||}$, varied from 0 mT to 200 mT, applied in the direction parallel to the substrate surface. The resulting differential conductance of the YSR state is plotted as a function of the source-drain bias and the strength of the magnetic field in Figure 4.17a using a DC measurement and in Figure 4.17b using a AC+DC measurement.

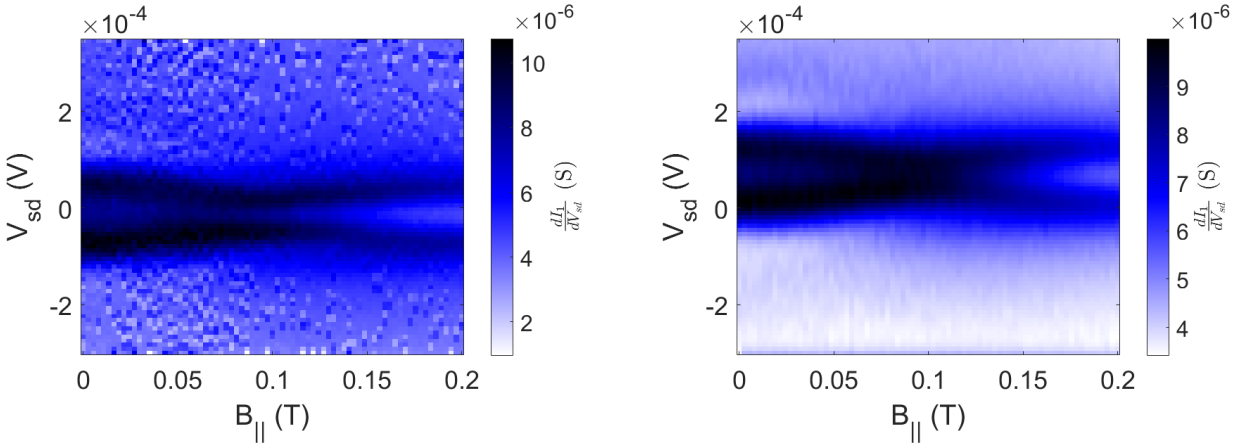


(a) DC measurement.

(b) AC+DC measurement.

Figure 4.17: Differential conductance, $\frac{dI_1}{dV_{sd}}$, as a function of source-drain bias, $V_{sd}$, and magnetic field, $B_{||}$.

The figures show how the YSR state changes with the magnetic field, but with an applied magnetic field, the superconducting gap should also be closing. The gap closes at around 100 mT, and after that the Zeeman splitting of the electron in the doublet state becomes visible. The Zeeman splitting was used to estimate the $|g^*|$-factor to approximately 10, according to Equation (2.25). The measurements in Figures 4.17a and 4.17b show a difference between the DC measurement and the AC+DC measurement. The YSR state is not centered around $V_{sd} = 0$ V in the AC+DC measurement, indicating a DC offset of approximately $0.83 \cdot 10^{-4}$ V between the lock-in amplifier and the voltage-to-current amplifier. It is also easier to distinguish the features in the DC measurement compared to the AC+DC measurement. This is more pronounced in Figure 4.18, where the two differential conductances have been plotted in the same figure, as functions of the source-drain voltage, for 100 mT and 200 mT. In these figures, the differential conductance for the AC+DC measurement has been shifted by $0.83 \cdot 10^{-4}$ V to compensate for the DC offset.

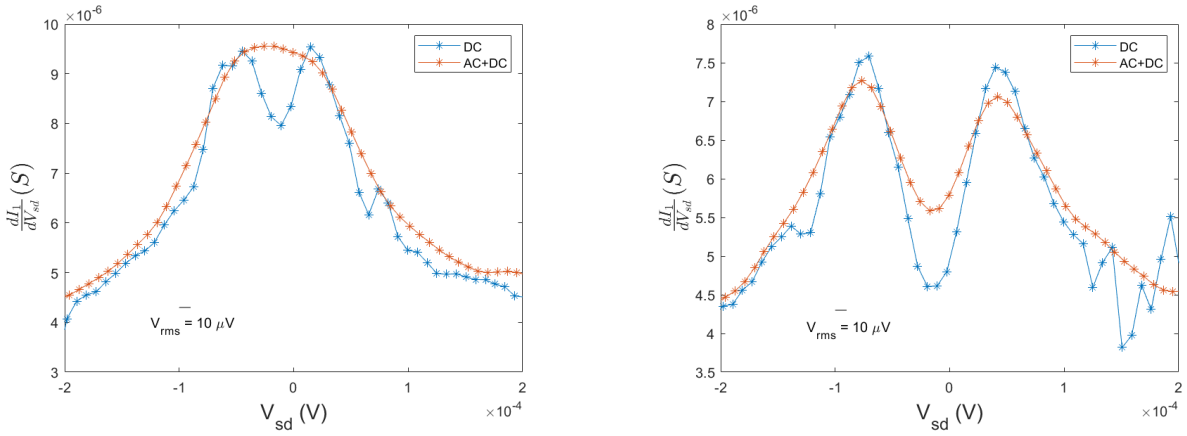


(a) 100 mT.

(b) 200 mT.

Figure 4.18: Differential conductance, $\frac{dI_1}{dV_{sd}}$, as a function of source-drain bias, $V_{sd}$. The differential conductance for the AC+DC measurement has been shifted by $0.83 \cdot 10^{-4}$ V to compensate for the DC offset. A horizontal line corresponding to the rms voltage used in the AC+DC measurement has also been indicated.

The figures show that the orange AC+DC curve is smoother than the blue DC curve and the peaks of Figure 4.18b have been compressed and less prominent than in the DC measurement. In Figure 4.18a, the smoothing of the curve in the AC+DC measurement has affected the resolution and it is no longer possible to distinguish the two peaks, which is a disadvantage of the AC+DC measurement. The spacing between the measurement points was approximately 8 µV both for the DC and the AC+DC measurement. The rms voltage, $V_{AC}$, was 10 µV and it is possible that a smaller $V_{AC}$ should be used such that $V_{AC} < 8$ µV. This might have resulted in a higher resolution in the AC+DC measurement, but no such measurement has been made.

Another disadvantage of the AC+DC measurement is that the differential conductance is measured directly. In the DC case, the current is measured, which later can be used to numerically calculate the differential conductance. This means that there is greater freedom in the DC measurements. For example, it is possible to apply different filter settings or change the number of points between which the differential conductance is estimated. There are of course many different settings that can be changed and filters that can be applied even in the AC+DC measurement, but to see the result of these, the entire measurement must be redone. It is important to mention that it is possible to use a current amplifier from which the signal can be split into a lock-in amplifier and a DC amplifier. In this way one can measure the current and the differential conductance simultaneously.

### 4.3.5 Cooper pair splitting

Figure 4.19 shows a DC measurement of the current through the two quantum dots, $I_1$ and $I_2$, as a function of $V_{bg}$ and $V_{sg}$. QD1 was kept in resonance by the back gate, while the side gate swept a level in QD2 in and out of resonance with the superconducting contact.

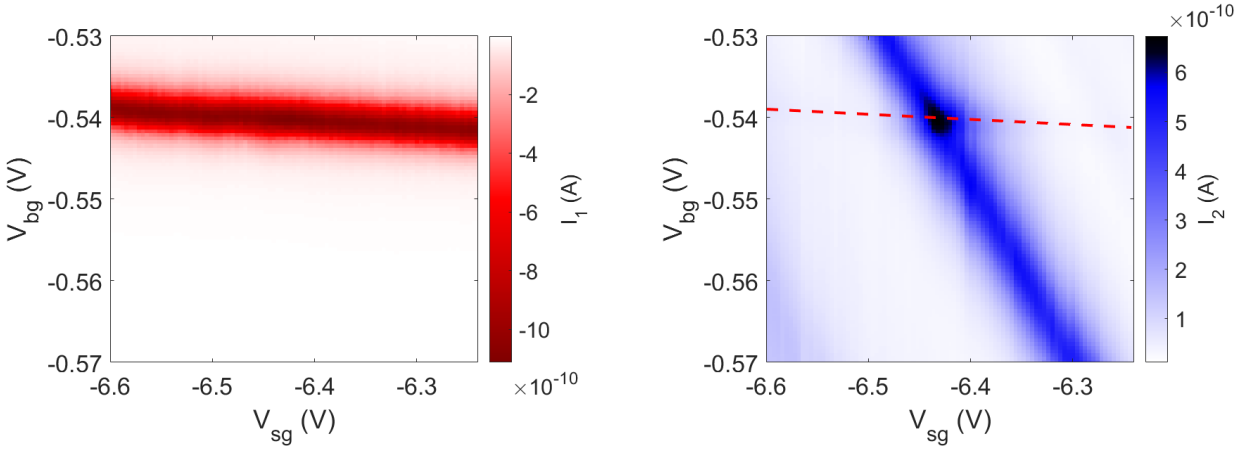


(a) QD1.

(b) QD2. Check current scale bar.

Figure 4.19: DC measurement. Currents, $I_1$ and $I_2$, as functions of back gate voltage, $V_{bg}$, and side gate voltage, $V_{sg}$.

It can be noticed that the direction of the current is different for the two quantum dots. This should indicate that electrons are tunneling into one of the normal contacts, while electrons are tunneling out of the other normal contact. By looking back to Figure 4.11, it is likely that electrons are pushed out from S to N2 since $\Delta\mu_2 = 70$ µeV. But, because $\Delta\mu_1 = -65$ µV, the electrons are likely pushed out from N1 to S. A red dashed line has been drawn to represent the resonance line for QD1. It seems that when both quantum dots are in resonance the current in QD2 increases. In this figure the color bar has also been changed to make it easier to distinguish. To see how much the current increased, the current was plotted along the resonance line of QD2. See Figure 4.20.

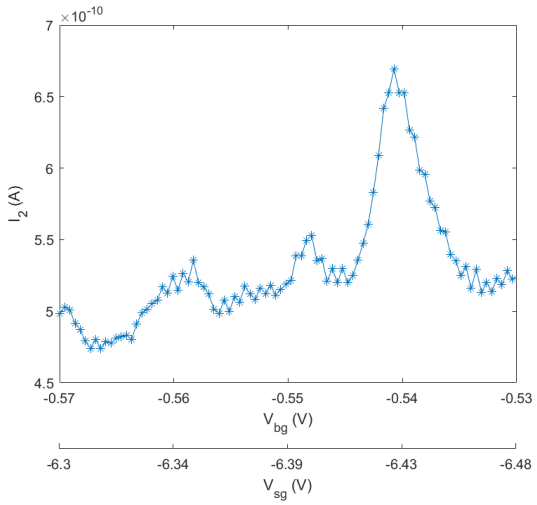


Figure 4.20: DC measurement. Current in QD2, $I_2$, along the resonance line.

There is a distinct peak, with 1.3 times larger current, when the two resonance lines intersect each other. In order to show that the increase in current is due to CPS, it is necessary to perform the same measurement again, but this time when the superconductivity is suppressed. In this control measurement, no current increase should be visible. The result from the measurement, with a magnetic field of $B_{||} = 250$ mT, applied parallel to the substrate surface, can be seen in Figure 4.21.

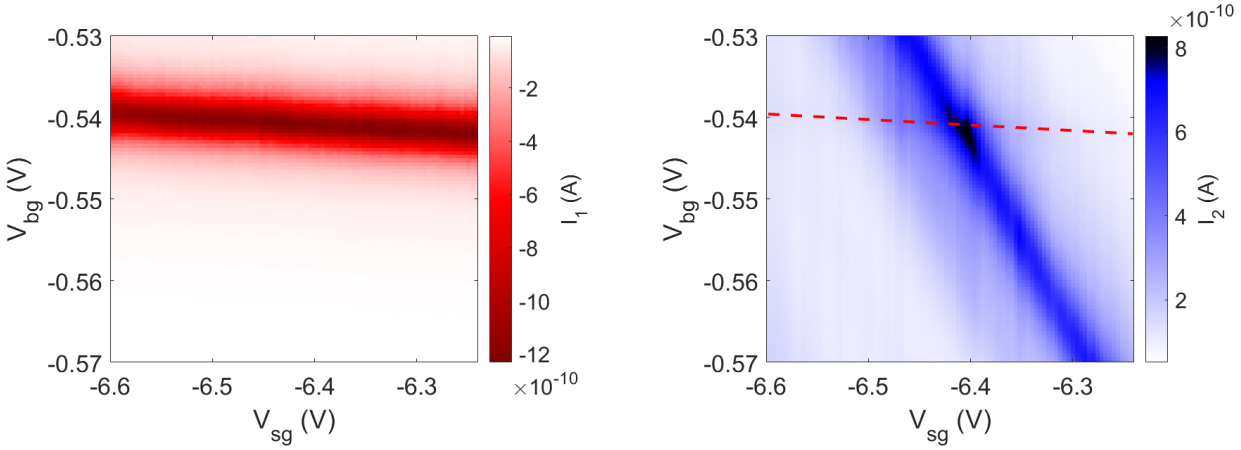


(a) QD1.

(b) QD2. Check current scale bar.

Figure 4.21: DC measurement. Current as function of back gate and side gate voltage. $B_{||} = 250$ mT.

It still seems that there is an increase in the current in QD2 when both quantum dots are in resonance. This would not be the case if it was due to CPS, since there now is a magnetic field of 250 mT applied, which should be large enough for the Ti/Al contact not to be superconducting. The question is why this false indication of Cooper pair splitting can be seen? Could this be because it is a DC measurement?

To be able to answer this question, the measurement with no applied magnetic field was performed again, but with the AC measurement technique. The result from this measurement can be seen in Figure 4.22. The reference frequency was 63.4 Hz, the rms voltage was 75 µV and the time constant was 300 ms. The measurement took 1 h and 33 min, in comparison with the DC measurement which took 54 min, using the same number of measuring points.

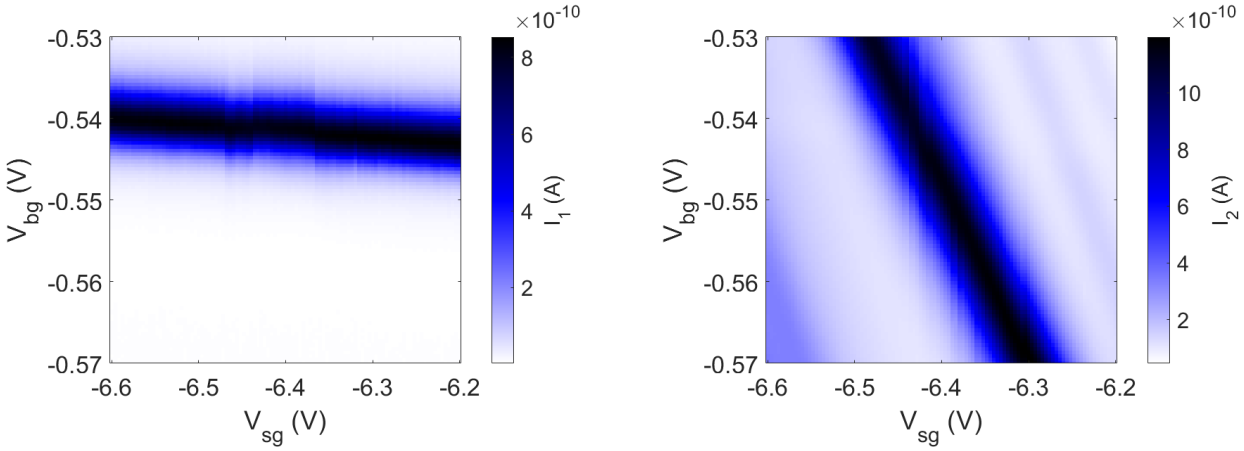


(a) QD1.

(b) QD2.

Figure 4.22: AC measurement. Current as function of back gate and side gate voltage. $B_{||} = 0$ mT.

By comparing the appearance of Figure 4.19b and Figure 4.22b, it is possible to see a difference between the DC and AC measurement. Now, there seems to be no increase in the current in QD2 when both quantum dots are in resonance. This indicates that the current peak seen for the DC measurement is in some way due to the fact that it is a DC measurement. One possible reason is that the current peak is caused by the large DC offset between the amplifiers. The superconducting contact is not a perfect voltage source and does not perfectly set the potential of the middle nanowire segment. Any current that flows will change the potential, so when a level in QD1 is in resonance with S, a current will flow from N1 to S through QD1, which would lead to a decrease in the potential difference between N1 and S. This potential decrease will result in an increase in the potential difference across QD2 and an increase in current.

Now another question must be answered, why is there no sign of Cooper pair splitting in the AC measurement, where there is no DC offset between the amplifiers? One possible reason is that the distance between the quantum dots is too long and the width of the superconducting contact is too large, compared to the relevant coherence lengths. Typical coherence lengths in thin aluminum nanostructures lie in the range of 100 to 200 nm and the coherence length in InAs nanowires is in the same order of magnitude. The distance between the quantum dots is approximately 550 nm and the width of the superconducting contact is approximately 400 nm. For comparison, the width of the superconducting aluminum contact is 200 nm in [10] and 150 nm in [11], which both have seen Cooper pair splitting. The width of the superconducting contact in this project is, therefore, twice as large as in [10].

### 4.3.6 Summary electrical measurements

In this thesis, several comparisons have been made between DC and AC measurements. DC measurements are simpler and do not require much optimization of settings to be suitable for a certain type of measurement. AC measurements, on the other hand, require that settings such as reference frequency and root-mean square voltage are selected appropriately. In this project, these settings have likely not been successfully selected, as the results have shown that the AC measurements resulted in broader Coulomb peaks with a lower maximum conductance than the corresponding DC measurements. These settings also affect the resolution and can limit which physical phenomena that can be studied, which was illustrated when a DC measurements and AC+DC measurements were compared to study a Yu-Shiba-Rusinov state.

One disadvantage with DC measurements is the presence of a possible DC offset between the amplifiers. This has proven to be a problem when studying Cooper pair splitting. The DC offset can make it impossible for the superconducting gaps to overlap each other. Should this happen, it will be very unlikely that there is any chance of detecting Cooper pair splitting. In addition, this DC offset may also give rise to non-local signals. If Cooper pair splitting is to be studied, AC measurements should be used due to a risk of detecting non-local signals not originating from Cooper pair splitting. The ultimate goal of this thesis was to detect Cooper pair splitting in InAs nanowires with crystal phase-defined quantum dots. This has not been achieved. The reason why no Cooper pair splitting has been detected is probably because the distance between the two quantum dots is too long.

# Chapter 5

# Conclusion and outlook

The work in this thesis is a first step towards the realization of CPS in InAs nanowires with crystal-phase defined quantum dots. Previous studies with these nanowires have shown that they seem promising towards a future development of spin-resolved CPS. In Ref. [18] a mechanism for spin and orbital manipulation using small electric and magnetic fields was presented, which was used to form nearly perfect quantum rings inside InAs nanowires with large and highly anisotropic effective g-factors. This mechanism can be used in future development of a possible spin filtering system. If this turns out to be possible this opens a route towards a test of the EPR paradox and Bell's inequality.

The quality of the InAs-Ti/Al contact interface became better if the whole GaSb shell was removed before any other process step, than if the GaSb was removed in two separate steps. However, there is still potential for improvement of the contact interface. To further improve the etching of GaSb, more studies should be conducted with more nanowires, different etching times and with a more reliable method to measure the diameter. In-situ argon or hydrogen milling should also be used to get a higher quality of the interface between the superconductor and the nanowire. In the future, the hydrochloric acid wet-etch performed to etch native oxides might also be replaced by an hydrogen fluoride wet-etch, which may attack GaSb to a greater extent. It is also interesting to find out if a better quality of the superconductor-nanowire interface can be obtained if the superconducting contact is defined before the normal contacts, to minimize nanowire degeneration caused by air exposure.

In this thesis, several comparisons have been made between DC and AC measurements. DC measurements are, in general, faster and simpler than AC measurements. In order to improve the AC measurements, more time should be spent in the future on optimizing the settings. A disadvantage with DC measurements is the presence of a possible DC offset between the amplifiers, which can create a non-local signal not originating from CPS. In future search for CPS, AC measurements should therefore be used. Something that was not investigated in this thesis was if it was possible to detect CPS with an AC+DC measurement technique.

The ultimate goal of this thesis was to detect CPS in InAs nanowires with crystal phase-defined quantum dots, but no Cooper pair splitting could be confirmed. This was probably because the distance between the quantum dots was too long. One disadvantage of crystal phase-defined quantum dots is that the output is largely dependent on the growth of the nanowires. If CPS can not be detected in future devices, it is possible that both the processing and the growth of the nanowires must be changed. In quantum dots defined with local gates, for example, it is possible to tune the coupling strength between the quantum dots and the contacts, which cannot be done with crystal phase-defined quantum dots. The advantages of the quantum dots studied in this thesis are, instead, that the quantum dots are very well defined and have shown promising signs of spin and orbital manipulation, which is a key component for future spin-resolved CPS.

# Bibliography


[1] A. Einstein, B. Podolsky, and N. Rosen, "Can quantum-mechanical description of physical reality be considered complete?", *Phys. Rev.,* **47**, 777 (1935).

[2] J. S. Bell, "On the Einstein Podolsky Rosen Paradox", *Physics*, **1**, 195 (1964).

[3] A. Aspect, "Bell's inequality test: more ideal than ever", *Nature*, **398**, 189 (1999).

[4] W. Tittel, J. Brendel, H. Zbinden, and N. Gisin, "Violation of Bell Inequalities by Photons More Than 10 km Apart",*Phys. Rev. Lett.,* **81**, 3563 (1998).

[5] G. Vidal, "Efficient Classical Simulation of Slightly Entangled Quantum Computations", *Phys. Rev. Lett.,*, **91**, 147902 (2003).

[6] K. Mattle, H. Weinfurter, P. G. Kwiat, and A. Zeilinger, "Dense Coding in Experimental Quantum Communication", *Phys. Rev. Lett.,*, **76**, 4656 (1996).

[7] D. Bouwmeester, J-W. Pan, K. Mattle, M. Eibl, H. Weinfurter, and A. Zeilinger, "Experimental quantum teleportation", *Nature,*, **390**, 575 (1997).

[8] A. K. Ekert, J. G. Rarity, P. R. Tapster, and G. M. Palma, "Practical Quantum Cryptography Based on Two-Photon Interferometry", *Phys. Rev. Lett.,*, **69**, 1293 (1992).

[9] Z. Scherübl, G. Fülöp, J. Gramich, A. Pályi, C. Schönenberger, J. Nygård, and S. Csonka, "From Cooper pair splitting to the non-local spectroscopy of a Shiba state", *arXiv*, arXiv:cond-mat.mes-hall/2108.12155v1, (2021).

[10] J. Schindele, A. Baumgartner, and C. Schönenberger, "Near-Unity Cooper Pair Splitting Efficiency", *Phys. Rev. Lett.,* **109**, 157002 (2012).

[11] L. Hofstetter, S. Csonka, J. Nygård, and C. Schönenberger, "Cooper pair splitter realized in a two-quantum-dot Y-junction", *Nature*, **461**, 960 (2009).

[12] G. Fülöp, S. d'Hollosy, A. Baumgartner, P. Makk, V. A. Guzenko, M. H. Madsen, J. Nygård, C. Schönenberger, and, S. Csonka, "Local electrical tuning of the nonlocal signals in a Cooper pair splitter", *Phys. Rev. B,* **90**, 235412 (2014).

[13] P. Recher, E. V. Sukhorukov, and D. Loss, "Andreev tunneling, Coulomb blockade, and resonant transport of nonlocal spin-entangled electrons,", *Phys. Rev. B,* **63**, 165314 (2001).

[14] G.B. Lesovik, T. Martin, and G. Blatter, "Electronic entanglement in the vicinity of a superconductor", *Eur. Phys. J. B*, **24**, 287 (2001).

[15] S. Baba, C. Jünger, S. Matsuo, A. Baumgartner, Y. Sato, H. Kamata, K. Li, S. Jeppesen, L. Samuelson, H. Q Xu, C. Schönenberger, and S. Tarucha, "Cooper-pair splitting in two parallel InAs nanowires", *New J. Phys.*, **20**, 063021 (2018).

[16] J. Klinovaja and D. Loss, "Time-reversal invariant parafermions in interacting Rashba nanowires", *Phys. Rev. B,*, **90**, 045118 (2014).

[17] A. Hutter and D. Loss, "Quantum computing with parafermions", *Phys. Rev. B,*, **93**, 125105 (2016).

[18] H. Potts, I.–J. Chen, A. Tsintzis, M. Nilsson, S. Lehmann, K.A. Dick, M. Leijnse, and C. Thelander, "Electrical control of spins and giant g-factors in ring-like coupled quantum dots", *Nat. Commun.*, **10**, 5740 (2019).

[19] C. W. J. Beenakker, "Theory of Coulomb-blockade oscillations in the conductance of a quantum dot," *Phys. Rev. B,* **44**, 1646 (1991).

[20] L. P. Kouwenhoven, C. M. Marcus, P. L. McEuen, S. Tarucha, R. M. Westervelt, and N. S. Wingreen, "Electron Transport in Quantum Dots", *Mesoscopic Electron Transport. NATO ASI Series*, **345**, 105 (1997).

[21] H. Potts, M. Leijnse, A. Burke, M. Nilsson, S. Lehmann, K. A. Dick, and C. Thelander, "Selective tuning of spin-orbital Kondo contributions in parallel-coupled quantum dots", *Phys. Rev. B,* **101**, 115429 (2020).

[22] M. Nilsson, *Charge and Spin Transport in Parallel-Coupled Quantum Dots in Nanowires*. Doctoral thesis, Lund University, (2018).

[23] M. Tinkham, *Introduction to superconductivity*, Dover Publications, ISBN: 0486435032, (2004).

[24] J. F. Annett, *Superconductivity, Superfluids and Condensates*, Oxford University Press, ISBN: 0198507569, (2004).

[25] H. K. Onnes, "The Superconductivity of Mercury", *Comm. Phys. Lab. Univ., Leiden*, 122 (1911)

[26] W. Meissner and R. Ochsenfeld, "Ein neuer Effekt bei Eintritt der Supraleitfähigkeit", *Naturwissenschaften*, **21**, 787 (1933).

[27] J. Bardeen, L. N. Cooper, and J. R. Schrieffer, "Theory of superconductivity," *Phys. Rev.*, **108**, 1175 (1957).

[28] L. N. Cooper, "Bound electron pairs in a degenerate fermi gas", *Phys. Rev.*, **104**, 1189 (1956).

[29] J. O. Schindele, *Charge and Spin Transport in Observation of Cooper Pair Splitting and Andreev Bound States in Carbon Nanotubes*. Doctoral thesis, University of Basel, (2014).

[30] C. Espy, O. J. Sharon, J. Braun, R. Garreis, F. Strigl, A. Shaulov, P. Leiderer, E. Scheer, and Y. Yeshurun, "Flux-periodicity crossover from h/2e to h/e in aluminium nano-loops", *J. Phys.: Conf. Ser.,* **969** 012063 (2018).

[31] S. A. Gebrehiwot, *Charge transport in InAs nanowire devices*. Doctoral thesis, Chalmers University of Technology, (2013).

[32] V. Koerting, B. M. Andersen, K. Flensberg, and J. Paaske, "Nonequilibrium transport via spin-induced subgap states in superconductor/quantum dot/normal metal cotunnel junctions", *Phys. Rev. B*, **82**, 245108 (2010).

[33] A. Jellinggaard, K. Grove-Rasmussen, M. H. Madsen, and J. Nygård, "Tuning Yu-Shiba-Rusinov states in a quantum dot", *Phys. Rev. B*, **94** 064520 (2016).

[34] A. Belabbes, C. Panse, J. Furthmüller, and F. Bechstedt, "Electronic bands of III-V semiconductor polytypes and their alignment," *Phys. Rev. B,* **86**, 075208 (2012).

[35] L. Namazi, M. Nilsson, S. Lehmann, C. Thelander, and K. A. Dick, "Selective GaSb radial growth on crystal phase engineered InAs nanowires," *Nanoscale,* **7**, 10472 (2015).

[36] C. Thelander, "Atomatic electrods", LabVIEW program, (2018).

[37] L. Hofstetter, S. Csonka, A. Baumgartner, G. Fülöp, S. d'Hollosy, J. Nygård, and C. Schönenberger, "Finite bias Cooper pair splitting", *Phys. Rev. Lett.,* **107**, 137801 (2011).

[38] Stanford Research Systems, manual for DSP Lock-In Amplifier model SR830 (1999).

[39] Femto Messtechnik GmbH, datasheet for Femto DLPCA-200 Variable Gain Low Noise Current Amplifier (2019).

[40] E. J. Lee, X. Jiang, M. Houzet, R. Aguado, C. M. Lieber, and S. De Franceschi, "Spin-resolved Andreev levels and parity crossings in hybrid superconductor-semiconductor nanostructures," *Nature Nanotechnology*, **9**, 79 (2014).

[41] J.-D. Pillet, C. H. L. Quay, P. Morfin, C. Bena, a. L. Yeyati, and P. Joyez, "Andreev bound states in supercurrent-carrying carbon nanotubes revealed", *Nat. Phys.*, **6**, 965 (2010).

[42] C. Jünger, S. Lehmann, K. A. Dick, C. Thelander, C. Schönenberger, and A. Baumgartner, "Intermediate states in Andreev bound state fusion," *arXiv*, arXiv:cond-mat.mes-hall/2111.00651, (2021).

# Appendix A

# Contact design

The LabVIEW program "Automatic electrodes" was used to create the electrode patterns for electron beam lithography. Some contacts were moved and redrawn in the program "Raith150". Figure A.1 shows the original SEM image of the nanowire for the device in Chapter 4, the contact design created in "Automatic electrodes", the original SEM image with the contact design superimposed and the final contact design created in "Raith150". All devices fabricated according to process 1 and process 2 were made in a similar way. Table A.1 shows a summary of the intended distances in the final design file compared to the actual distances for the device, measured from Figure 4.5b.

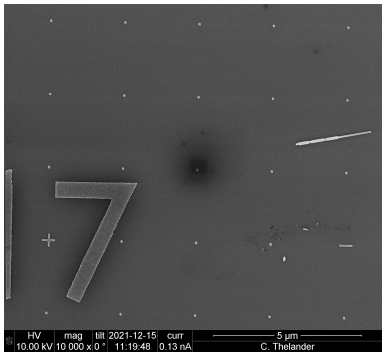


(a) SEM image of the nanowire.

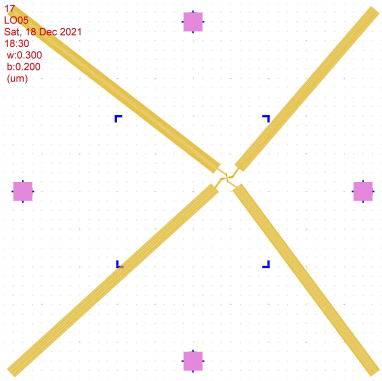


(b) Design file created in "Automatic electrodes".

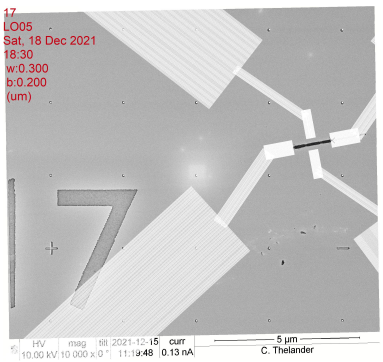


(c) SEM image with design file superimposed.

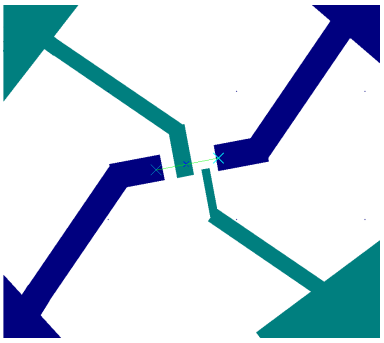

(d) Final design file created in "Raith150" and used for EBL exposure.

Figure A.1: The four steps in the contact design process for the device in Chapter 4.

Table A.1: The indented and actual distances for the device in Chapter 4 and the difference between the intended and actual distance. An EBL offset of -50 nm in the x-direction was accounted for. All distances are in nm.

| | **Intended distance** | **Actual distance** | **Difference** |
|---|---|---|---|
| Thickness of sg | 150 | 220 | +70 |
| Thickness of N1 | 500 | 590 | +90 |
| Thickness of N2 | 500 | 570 | +70 |
| Thickness of S | 330 | 400 | +70 |
| Distance between N1 and N2 | 1070 | 890 | -180 |
| Distance between S and N1 | 260 | 160 | -100 |
| Distance between S and N2 | 480 | 340 | -140 |
| Distance between S and sg | 170 | 90 | -80 |
| Distance between sg and N2 | 170 | 100 | -70 |

What can be seen from the table is that all contacts became thicker than intended and all distances between different contacts became shorter. This is due to resolution limits in the EBL system. The choice of exposure parameters for EBL, which can be seen below, affects the resolution.

**Exposure parameters for electron beam lithography**

- Acceleration voltage: 20 kV
- Area dose: 260 µC/cm$^2$
- Working distance: 6 mm
- Aperture size: 20 µm.

# Appendix B

# Etching of GaSb along point B and C

The result from the etching measurements along point B and C can be seen in Figure B.1. The values on the x-axis indicate which nanowire is being measured. All figures are divided into three sections corresponding to $H_2O$ 30 min, MF319 30 min and MF319 3 min. Figures B.1a and B.1c show the diameter of the nanowire along point B and C before and after etching, with an estimated sample standard deviation of $s_d = 4.7$ nm. Figures B.1b and B.1d show the diameter difference, calculated as the diameter before - the diameter after, on the nanowire along point B and C, with an estimated sample standard deviation of $s_\Delta = 6.6$ nm. In Figures B.1b and B.1d, three horizontal lines have also been drawn. The middle line corresponds to the mean value of the measuring points, while the two dashed lines correspond to the mean value $\pm$ $s_\Delta$.

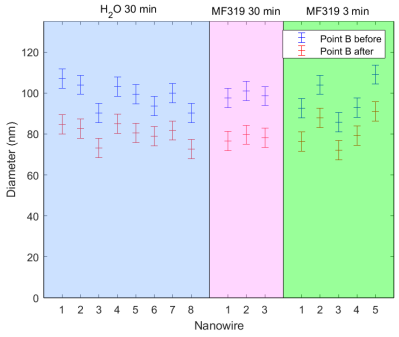


(a) Diameter before (blue) and after (red) etching for point B.

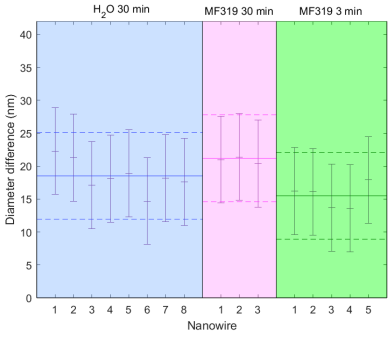


(b) Diameter difference for point B. The horizontal lines show the average diameter difference.

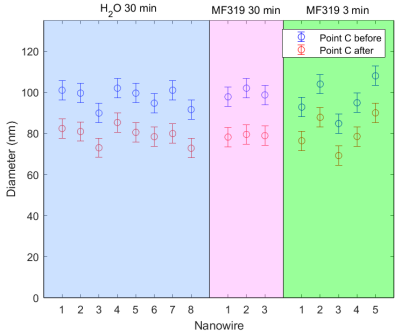


(c) Diameter before (blue) and after (red) etching for point C.

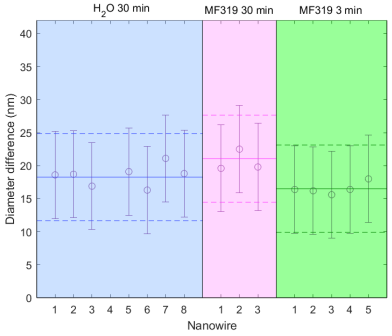


(d) Diameter difference for point C. The horizontal lines show the average diameter difference.

Figure B.1: Etching results along point B and C.

# Appendix C

# Error estimation

Let $X_c$ = [134 nm 136 nm 138 nm 142 nm] be the distribution of FWHM values along the same horizontal line obtained from different contrast and brightness settings in Figure 3.11. The sample standard deviation of this distribution, $s_c$, was calculated to 3.4 nm according to,

$$s_c = \sqrt{\frac{\sum_{i=1}^{n_c}(X_{ci} - \bar{X_c})^2}{n_c - 1}}, \tag{C.1}$$

where $X_{ci}$ is the $i$'th value, $\bar{X_c}$ is the mean value and $n_c$ is the number of values in $X_c$. In the same way, the sample standard deviation, $s_m$, was calculated to 3.1 nm for the distribution $X_m$ = [189 nm 191 nm 195 nm] of FWHM values along the same horizontal line obtained from different magnifications in Figure 3.12. It was also important that the chosen line across the nanowire was perpendicular to the nanowire growth direction. Note that this uncertainty depends on the diameter measured, where a thicker diameter gives a higher uncertainty. For simplicity, this uncertainty has been assumed to give the same error regardless of diameter with a roughly estimated standard deviation of $s_p = 1$ nm. By taking all three sources of error into account, the sample standard deviation for the diameter of the nanowires, $s_d$, was obtained as,

$$s_d = \sqrt{s_c^2 + s_m^2 + s_p^2} = 4.7 \text{ nm}. \tag{C.2}$$

The sample standard deviation for the diameter difference, $s_\Delta$, was obtained in the same way,

$$s_\Delta = \sqrt{s_d^2 + s_d^2} = 6.6 \text{ nm}. \tag{C.3}$$

Note that the uncertainties in the measurements are only roughly estimated. For future measurements, measures to reduce these sources of error should be considered. One way to reduce the error is to make sure to use the same SEM settings and the same magnification in all SEM images. Another suggestion to increase the accuracy of the measurements is to write a computer program that normalizes the contrast in the various SEM images. It is also possible to write a computer program that calculates the angle between the nanowire and the selected line to make it easy to ensure that the diameter is measured perpendicular to the nanowire growth direction.